Korean J. Chem. Eng., 39(3), 736-759 (2022)
DOI: 10.1007/s11814-021-0904-3

pISSN: 0256-1115
eISSN: 1975-7220

Study of rice husk ash derived MCM-41-type materials on pore expansion, Al incorporation, PEI impregnation, and CO_2 adsorption

Xu Zhang*, and Tao Du*,†**

*State Environmental Protection Key Laboratory of Eco-Industry, School of Metallurgy, Northeastern University, Shenyang, 110819, P. R. China
**Simulation Center, Shenyang Institute of Engineering, Shenyang, 110136, P. R. China
(*Received 21 April 2021 • Revised 25 June 2021 • Accepted 12 July 2021*)

Abstract−Conventional MCM-41 (M41), silica-pure pore-expanded MCM-41 (PM41), and Al-containing pore-expanded MCM-41 (PM41Ax) were synthesized from rice husk ash and tested as polyethyleneimine (PEI) supports for CO_2 capture. Samples were characterized by small-angle X-ray diffraction, X-ray fluorescence spectroscopy, scanning electron microscopy, Fourier transform infrared spectroscopy, granulometric analysis, and nitrogen adsorption techniques. The PEI loading rate and CO_2 adsorption-desorption performance were determined via thermogravimetric analysis. The effects of pore expansion, heteroatom Al incorporation, PEI loading rate, and Si/Al ratio on CO_2 adsorption performance were examined. For the first time, the amount of PEI impregnated in PM41 was increased beyond 55 wt%, and the low-Si/Al-ratio PM41Ax support was used to load PEI in a novel procedure. Results show that at the same PEI loading rate, PM41 is always superior to M41 regarding adsorption capacity and adsorption rate. For a PEI loading rate >50 wt%, the superiority is amplified, reaching 15.9% and 21.3%, respectively. The use of the high-Al-containing PM41Ax support further increases adsorption capacity and adsorption rate by 13.4% and 9.6%, respectively. The presented reaction has a hybrid adsorption characteristic that includes both chemisorption and physisorption. Avrami's fractional-order kinetic model describes the adsorption best. Over the entire time scale, the adsorption rate is determined by several kinetic diffusion-controlled processes. The intraparticle diffusion and equilibrium adsorption are two predominant rate-limiting steps, and their control ranges change with temperature. After five cycles of adsorption and desorption, the desorption ratio was as high as 99%, and the working capacity still retained 96.5% of the original capacity. In addition, the presence of water vapor increased the adsorption capacity of the adsorbents presented in this study. These advantages make them successful iin capturing CO_2 in the post-combustion scenario.

Keywords: Rice Husk Ash, MCM-41-type Material, Pore Expansion, Heteroatom Al Incorporation, Carbon Dioxide Adsorption

INTRODUCTION

Ever-increasing CO_2 emissions have increased the earth's average temperature by 2-3 °C, leading to accelerated glacier melting, rising sea levels, and more frequent environmental extremes such as unprecedented wildfires across Australia, a record-breaking Atlantic hurricane season, and a worldwide locust plague. However, we have never paid as much attention to CO_2 emissions as we do today. Although the coronavirus pandemic prevents face-to-face international climate conferences, several countries have been communicating via video conferencing to strengthen their climate action-related efforts for achieving carbon neutrality by 2050 for Japan and 2060 for China. However, fossil fuels will continue to dominate global energy in future decades. Consequently, establishing a CO_2-capture technology that is both practicable and economically viable is important.

Among multiple CO_2 capture techniques, adsorption has been identified as promising because of its low cost, simplicity, and maneuverability [1]. The immobilization of amine-containing substances in the pores of porous solids to provide CO_2 solid adsorbents, i.e., CO_2 "molecular basket," is common. This immobilization can completely utilize the ample internal space to uniformly disperse affinities in pores, thereby facilitating their efficient utilization. This attractive CO_2 solid adsorption technology has sparked widespread interest with an astonishing 2000 studies published between 2011 and 2014 [2]. Activated carbon [3], zeolites [4-6], metal-organic frameworks (MOFs) [7,8], polymers [9], clays [10], TiO_2 [11,12], nanotubes [13,14], silica gel [15], aerogel [16], and other porous solids have been successfully used as supports in previous studies. Among these candidates, after its first discovery by Mobil Corp. in 1992, MCM-41, a periodic silica-based molecular sieve with a highly ordered 2D hexagonal mesoporous structure, has gained considerable attention [17]. It is an excellent candidate for CO_2 capture because of its high specific surface area (>1,000 $m^2\ g^{-1}$), adjustable nano-scale pore size (2-10 nm), large pore volume (~1 $cm^3\ g^{-1}$), easily doped amorphous pore wall, and massive surface-modifiable hydroxyl groups.

Multiple amine-containing substances, including monoamines [18,19], diamines [20,21], triamines [22-26], tetraamines and multiple amines [27-29] have been successfully deposited on MCM-

†To whom correspondence should be addressed.
E-mail: dutao1964@hotmail.com

41-type materials. Because their adsorption performance is highly associated with the surface density of amine groups, multiple amine species are frequently preferred for designing adsorbents. Polyethyleneimine (PEI), a polymer with a repeating unit composed of an amine group and a two-carbon aliphatic chain CH_2CH_2, can be loaded on MCM-41-type materials via physical impregnation using either methanol or ethanol as a solvent. To our best knowledge, Xu et al. [27] reported the first instance of using PEI-impregnated MCM-41-type materials for CO_2 capture. After 150 min of exposure to pure CO_2 atmosphere at 75 °C, they achieved an adsorption capacity of 215 mg of CO_2 per gram of PEI using M41 impregnated with 50 wt% PEI, which was 24 times higher than M41 alone and twice that of pure PEI. Recently, Chen et al. [30] used M41 impregnated with 50 wt% PEI to achieve an uptake of ~117 mg of CO_2 per gram of adsorbent on exposure to 30 mL min^{-1} of pure CO_2.

In addition to surface amine density, pore size and volume are the second-most studied parameters relevant to adsorption performance because of the decision tree of Yıldız et al. [31] who pooled 1039 aminated MCM-41 and SBA-15 materials to examine various adsorption-relevant factors. Pore expansion treatment is effective for certain amine-containing species. For example, Franchi et al. [32] demonstrated that PM41 could accommodate additional diethanolamine (DEA), resulting in a higher CO_2 adsorption capacity than that of M41. Under the same adsorption conditions, Harlick et al. [25] found that the CO_2 adsorption capacity of TRI-grafted PM41 was significantly higher than that of TRI-grafted M41. However, a comparison of different studies reveals that PEI-impregnated PM41 does not show any superiority in CO_2 adsorption. Heydari et al. [33] used PM41 impregnated with 55 wt% PEI to capture 89.1 mg of CO_2 per gram of adsorbent in the presence of pure CO_2 at 75 °C, which was lower than the capture amount (112 mg of CO_2 per gram of adsorbent) achieved by Xu et al. [27] using M41 impregnated with 50 wt% PEI. Compared to PM41, M41 is apparently the more appropriate PEI support. However, the abovementioned adsorbents were prepared under different experimental conditions and then exposed to CO_2 streams of varying concentration and flow rate. Consequently, determining M41 as the better PEI support under these conditions with many differences is debatable. Furthermore, intuitively, a solid with a larger pore size and pore volume can load additional PEI. To date, the maximum amount of PEI impregnated on PM41 in the existing data has been only 55 wt%, considerably lower than that (75 wt%) of M41. Therefore, these studies comparing PM41-supported PEI for CO_2 capture with their M41 counterparts are neither systematic nor comprehensive.

Furthermore, as per Xu et al. [34], the incorporation of heteroatom Al within the M41 framework was beneficial for CO_2 adsorption, and the lower the Si/Al molar ratio of the M41 support, the higher the capacity of the M41 PEI adsorbent. The adsorption of PEI-impregnated pure Si-based M41 was 12% higher when the Si/Al molar ratio was 100. The increased CO_2 adsorption was attributed to higher pore volume when the framework was replaced. However, their study's lowest Si/Al ratio was only 100, and the impact of a higher Al content on CO_2 adsorption has yet to be investigated.

A commercially competitive adsorbent must possess multiple adsorption-desorption stability, moderate regeneration conditions, and low regeneration energy consumption, in addition to high adsorption and fast adsorption kinetics. Pressure swing adsorption (PSA) and temperature swing adsorption (TSA) are two well-known CO_2 removal and recovery technologies [35,36]. To date, they have achieved commercial success in natural gas sweetening, H_2 purification, and the elimination of volatile organic compounds. However, for a CO_2 post-combustion capture scenario suitable for treating coal-fired power plant flue gas, the most prevalent anthropogenic CO_2 emission source, PSA is somewhat commercially unacceptable because of its excessively enlarged footprint: 13,285 m^2 for an advanced supercritical pulverized coal unit, which is ~50 times that of chemical absorption based on MEA [37]. However, TSA is better because it saves mechanical power and recovers high-purity CO_2 via indirect heating [38]. In the literature, lab-scale regeneration of CO_2-loaded MCM-41-based adsorbents is primarily achieved by purging with inert gas (typically N_2) at temperature higher than that of adsorption, i.e., by TSA [27,32]. However, at a single desorption temperature, the majority of desorption studies focus on cyclic adsorption-desorption stability. In terms of desorption, Raganati et al. [39] provided an excellent in-depth analysis of CO_2 desorption from CB-FM in terms of desorption temperature, desorption capacity, and kinetics. This is what MCM-41-based adsorbents lack in terms of CO_2 desorption.

To date, various low-cost silica precursors have been developed for preparing MCM-41-type materials, which can be divided into two categories: (i) silica-containing natural minerals such as natural clay [40], microcline [41], metakaolin [42], kaolin [43], halloysite [44], K-feldspar [45], bentonite [46], and diatomite [47], and (ii) anthropogenically produced silica-bearing waste solids such as fly ash [48], coal slag [49], spent glass [50], photonic waste powder [51], rice husk ash [5], resin [52], peanut shell ash [53], and wheat straw ash [54]. Rice husk is one of the world's most abundant agricultural wastes. Farmers frequently burn it, which produces hazardous fumes, inhalable particulate matter, and dispersed dust [55]. Hence, preparing MCM-41 using rice husk has considerable economic and environmental benefits. Furthermore, the silica purity of rice husk extract is as high as 98% [5], which is difficult to achieve with other solid wastes. The resulting rice husk-derived MCM-41 is practically impurity-free, allowing for improved control of subsequent adsorbent composition, structure, and morphology.

Based on the above analysis, we synthesized M41, PM41, and PM41Ax from rice husk ash, and then loaded them with PEI to produce MCM-41-type adsorbents for CO_2 capture. This study evaluated the effect of pore expansion treatment, incorporation of heteroatom Al, PEI loading rate, and Si/Al atomic ratio on CO_2 adsorption performance via a systematic and comprehensive approach, as well as to uncover the adsorption mechanism, determine the rate-limiting factor, and highlight the application of high-Al-content PM41Ax in CO_2 capture technology.

EXPERIMENTAL

1. Reagents and Materials

All chemical reagents were analytically pure and used as-received without treatment. NaOH, CH_3OH, CH_3CH_2OH, $NaAlO_2$, 25 wt%

NH_3, concentrated HCl, glacial CH_3COOH, and cetyltrimethylammonium bromide (CTAB) were purchased from Sinopharm, while PEI and 1,3,5-trimethyl benzene (TMB) were purchased from Aladdin. We obtained the rice husk from a local farm.

2. Si Extraction from Rice Husk

SiO_2 was extracted via the extraction procedure used in our previous study [5]. Typically, rice husk was heated at 700 °C for 6 h to obtain rice husk ash (RHA). Then, the as-synthesized RHA was chemically treated with 2.5 mol L^{-1} of NaOH and concentrated HCl successively. Finally, we recovered the SiO_2 precipitate via filtration, rinsed it with copious amounts of deionized water, and dried it overnight at 90 °C. Table 1 lists the X-ray fluorescence (XRF) analysis, which shows that the SiO_2 purity is as high as 98.6 wt%.

3. Preparation of MCM-41-type Materials

PM41Ax materials were prepared using a one-pot hydrothermal method, as previously described by Ziaei et al. [56]. First, we dissolved a specified amount of CTAB in deionized water at 40 °C and then agitated the mixture. Subsequently, the flocculent solution became translucent. RHA, NaOH, 25 wt% NH_3, $NaAlO_2$, and deionized water were added in succession to prepare the solution with the molar ratio of Si : CTAB : Na : NH_3=1 : 0.2 : 0.2 : 1.4 : 120 and Si/Al atomic ratios of 20, 30, and 40, respectively. The pH of the mixture was adjusted to ~10.5 by adding an aqueous solution of CH_3COOH. After an additional 30 min of agitating the mixture, a fixed amount of TMB used as a swelling agent was added as per the TMB/Si mass ratio of 1.5. After another 4 h of continuous agitation, the gelatinous solution was transferred to a Teflon-lined stainless autoclave to be crystallized at 110 °C for 72 h. Then, we recovered the white precipitate via filtration using copious amounts of deionized water, dried overnight at 90 °C, and heated at 550 °C for 5 h (ramping rate of 2 °C min^{-1}), resulting in a template- and sweller-free PM41Ax. For comparison, M41 and PM41 were synthesized using a similar procedure.

4. PEI Impregnation

The PEI-loaded adsorbent was prepared using a wet-impregnation method [5]. Typically, 1 g of as-calcined support was dispersed in 10 mL of methanol, followed by adding desired amounts of PEI. The resultant slurry was stirred for 15 min, transferred to a petri dish, and heated at 70 °C until methanol was completely evaporated, which resulted in the expected adsorbent, denoted as PM41Ax-yP, where x represents the molar ratio of Si/Al and y represents the PEI percentage weight in the adsorbent. Thus, the adsorbents built on M41 and PM41 are denoted as M41-yP and PM41-yP, respectively.

5. Characterization

To obtain the actual molar ratio of Si/Al, X-ray fluorescence (XRF) spectra were obtained using a Shimadzu XRF1700 version, which was used for the chemical composition analysis of Al-containing supports. To determine textural properties, an XRD-7000 X-RAY diffractometer (SHIMADZU, Japan) with CuKα radiation operated at 40 kV and 200 mA was used to record small-angle X-ray diffraction patterns (SXRD) for all the supports in the 2θ range of 0.5°-10° with a 0.02° step length and a 1 s step time. Nitrogen adsorption-desorption isotherms at −196 °C were measured on a JWBK112 volumetric analyzer (JWGB, China) to examine porosity characteristics. Prior to each measurement, the samples with and without PEI were vacuum activated for 2 h, respectively, at 105 and 150 °C to remove the pre-absorbed moisture and gas. The specific surface area (S_{BET}) was then determined by the Bruanuer-Emmett-Teller (BET) method using an isothermal adsorption branch in the relative pressure range of p/p_0=0.05-0.3, and the pore size distribution was obtained using the Barrett-Joyner-Halenda model. Total pore volume was then calculated from the N_2 amount adsorbed at a relative pressure of 0.99. To observe the morphology and evaluate the particle size, scanning electron microscopy (SEM) images were obtained using a Hitachi Cold Field Emission SEM (SU-8010 series). The particle size of the adsorbent was determined via nano-scale scanning using a Litesizer 500-type laser granulometer. Fourier transform infrared (FTIR) spectra were obtained between 4,000 and 400 cm^{-1} using an Agilent Cary 600 Series FTIR Spectrometer. The actual loading amount of PEI was determined using thermogravimetric analysis (TGA) on an STA-409 PC Lux thermogravimetric analyzer (NETZSCH, Germany). For each measurement, 10 mg of the sample to be tested was exposed to a 100 mL min^{-1} of Ar flow with a heating rate of 10 °C min^{-1} for up to 600 °C.

6. CO_2 Adsorption-desorption Measurements

CO_2 adsorption-desorption measurements were conducted on a thermogravimetric analyzer (NETZSCH, Germany). Typically, 10 mg of adsorbent was pretreated in a 100 mL min^{-1} flow of Ar at 75 °C for 60 min, and then exposed to a pure CO_2 stream at 100 mL min^{-1} at 75 °C for 120 min. Thus, the amount of CO_2 adsorbed was determined from the mass increment in the overall adsorption process. In terms of the adsorption rate, we implemented three different definitions as follows: i) the instantaneous adsorption rate, characterized by the ratio of mass gain to the spent time using the uptake-against-time data obtained in the TGA experiment; ii) linearized adsorption rate, characterized by the slope of adsorption curve at the initial time, indicative of how fast the adsorption process occurred, because of the accomplishment of most of the total uptake over CO_2 being within the first several minutes of contact time [34,57,58], and iii) self-equilibrium rate, i.e. the kinetic adsorption rate constant, although not the real adsorption rate, capable of presenting the result at which adsorption process would reach equilibrium first by comparing rate constants derived from the same kinetic model.

Then, we selected the best performing adsorbent in terms of adsorption capacity and adsorption rate for further studying the temperature dependence of adsorption (25, 50, 75, and 100 °C).

In terms of desorption, we exposed loaded adsorbents to a 100 mL min^{-1} of flowing pure Ar stream for 120 min, and evaluated the temperature dependence of desorption (75, 85, 95, and 105 °C), desorption kinetics, and cycle stability.

Note that CO_2 adsorption capacity or uptake in this study is the amount of CO_2 adsorbed per gram of adsorbent, while PEI efficiency, to be mentioned afterwards, refers to the CO_2 uptake based on per gram of PEI. Thus, they had the following relationship:

$$\begin{aligned}&CO_2 \text{ adsorption capacity/uptake}\\&=CO_2 \text{ adsorption capacity/uptake by support itself}\\&\times\text{percentage mass of support in adsorbent}\\&+\text{PEI efficiency}\times\text{percentage mass of PEI in adsorbent}\end{aligned} \quad (1)$$

7. Kinetics Study

To estimate the overall adsorption rate and to describe the adsorption-desorption behavior, we used the pseudo-first-order, pseudo-second-order, and Avrami's fractional-order kinetic models. Their mathematical expressions in the integrated form are listed below.

Pseudo-first-order kinetic model:

$$q_t = q_e[1-\exp(-k_1 t)] \quad (2)$$

Pseudo-second-order kinetic model:

$$q_t = \frac{k_2 q_e^2 t}{1+k_2 q_e t} \quad (3)$$

Avrami's fractional-order kinetic model:

$$q_t = q_e[1-\exp(-(k_A t)^{n_A})] \quad (4)$$

where q_t (mmol g^{-1}) and q_e (mmol g^{-1}) are the CO_2 uptakes at time t and equilibrium, respectively; k_1 (min^{-1}), k_2 (g $mmol^{-1}$ min^{-1}), and k_A (min^{-1}) are their kinetic rate constants; and n_A is Avrami's exponent.

To summarize, the pseudo-first-order kinetic model is suitable for describing the weakly connected and easily separated physisorption. However, the pseudo-second-order kinetic model can represent stably built and irreversible chemisorption [59]. Avrami's fractional-order kinetic mode was designed for describing particle nucleation. Therefore, it has been found suitable for predicting adsorption with more than one reaction pathway, e.g., a combination of chemisorption and physisorption [39].

After kinetic rate constants under different temperatures are obtained, the activation energy, characterized by the minimum energy required for an adsorbed adsorbate to detach from the adsorbent, can be obtained by applying the Arrhenius equation [60].

$$k = \exp\left(-\frac{E_a}{RT}\right) \quad (5)$$

where E_a (kJ mol^{-1}) is the activation energy, *A* is the Arrhenius pre-exponent, R is the universal gas constant (8.314 J mol^{-1} K^{-1}), and T is the temperature in Kelvin (K).

In addition to using the apparent kinetics models, we employed the three kinetic diffusion-controlled models to obtain the intrinsic determinants of adsorption rate.

Interparticle diffusion model (Fick's diffusion model): This model considers the resistance encountered by CO_2 when diffusing within the gap between adsorbent particles, i.e. interparticle diffusion resistance, as the rate-limiting step. It can be simplified as follows when $q_t/q_e>0.7$ [39,61].

$$1-\frac{q_t}{q_e} = \frac{6}{\pi^2}\exp\left(-\pi^2\frac{D_c}{r_p^2}t\right) \quad (6)$$

where t_D (min^{-1}) can be determined by solving the slope of the linearized form of Eq. (6), the ratio of q_t to q_e is the relative uptake, and the combination variable D_c/r_p^2 is the diffusion time constant.

If the value of the intercept of the fitted line equals $\ln(6/\pi^2)$, the interparticle diffusion is the rate-governing step; otherwise, other factors also dominate the reaction rate.

To obtain the diffusion time constant, the pseudo-first-order kinetic rate constant can be used provided all particles are equivalent to spheres of an identical size [23]. The mathematical expression is given by Eq.(7)

$$k_1 = 15 t_D \quad (7)$$

If the values of t_D from two different models, i.e., the interparticle diffusion model and the pseudo-first-order kinetic model, are equal, we can conclude that the interparticle diffusion resistance controls the reaction rate. Otherwise, other parameters may play non-negligible impacts on rate control.

Intraparticle diffusion model (Webber-Morris model): This model presumes that the diffusion resistance within the pores of adsorbents, i.e., intraparticle diffusion resistance, governs the reaction rate. Based on its intrinsic mechanism, it is suitable for describing adsorption on porous-structured adsorbents. Its approximated expression is given in Eq. (8).

$$q_t = k_{id} t^{1/2} + A \quad (8)$$

where k_{id} (mmol g^{-1} $min^{-0.5}$) is the intraparticle diffusion rate constant and *A* is a constant related to the thickness of the boundary layer.

We can acknowledge the role of intraparticle diffusion in rate control by observing the plot of q_t versus $t^{1/2}$, which is a straight line either going through the origin or not, indicating a solely governing role or a crucial but not unique role [62]. However, the most frequently observed case is that the plot is not a straight line but can be divided into three linear segments, corresponding to film/boundary diffusion, intraparticle diffusion, and equilibrium adsorption stage.

Boyd's films-diffusion model: This model assumes that the penetration resistance through the gas film surrounding the adsorbent, i.e., film-diffusion resistance, is the rate-limiting step for CO_2 adsorption. The mathematical expression is given by Eq. (9).

$$B_t = \begin{cases} -0.4977 - \ln(1-F), & F>0.85 \\ \left(\sqrt{\pi} - \sqrt{\pi - \left(\frac{\pi^2}{3}F\right)}\right)^2, & F<0.85 \end{cases} \quad (9)$$

where F is the uptake ratio of q_t to q_e.

Because the plot of B_t versus t is a straight line that passes through the origin, the intraparticle diffusion solely dominates the reaction rate, unless other processes such as film diffusion impact the reaction rate [63].

RESULTS AND DISCUSSION

1. Characterization

Fig. 1 shows the structural profiles of M41, PM41, and PE41Ax (x=20, 30, and 40) characterized by SXRD. Concerning M41, there are four distinct representative diffraction peaks at the value of 2θ below 10°, corresponding to the *hkl* panels of (100), (110), (200), and (210), respectively, indicative of highly resolved M41 [52]. After pore expansion treatment, the major characteristic diffraction peaks *hkl*=100 of all pore-expanded samples were noticeable but shifted to smaller angles. Moreover, the number of representative diffraction peaks decreased, e.g., only one for PM41Ax and two for PM41, as shown in Fig. 1. These phenomena indicate that despite the preservation of MCM-41-type structure, after pore expansion treat-

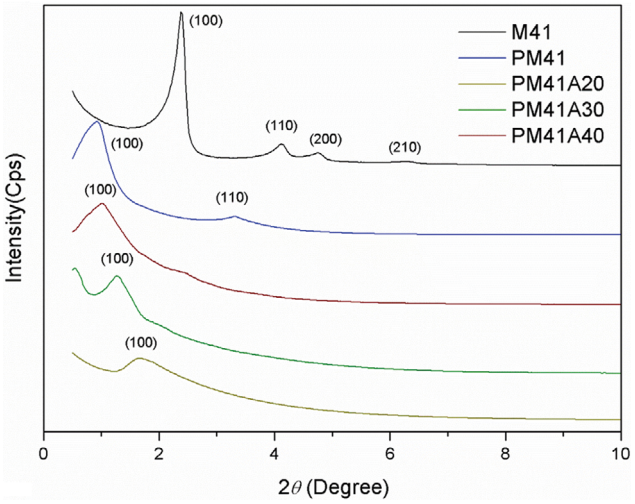

Fig. 1. SXRD profiles for M41, PM41, and PE41Ax (x=20, 30, and 40).

ment using the swelling agent TMB, the pore uniformity decreased consistently as reported in Jana et al. [64].

Table 1 lists the textural parameters of multiple samples in this study, which were characterized by XRF, SXRD, and N_2 isotherms. Both PM41 and PM41Ax have 1.7-2.0 times the pore diameter (d_{BJH}) and 1.3-1.5 times the pore volume (V_P) of M41, but lose 10.6%-20.4% of specific surface area (S_{BET}). Moreover, the actual Si/Al atomic ratios of PM41Ax are considerably close to the nominal ones given in parentheses, indicating that almost all Al atoms were successfully incorporated into the silica-based framework.

Fig. 2(a) shows the profiles of N_2 isotherms and BJH pore size distributions for M41, PM41, and PM41Ax (x=20, 30, and 40). M41 shows a typical type-IV isotherm as per the IUPAC classification.

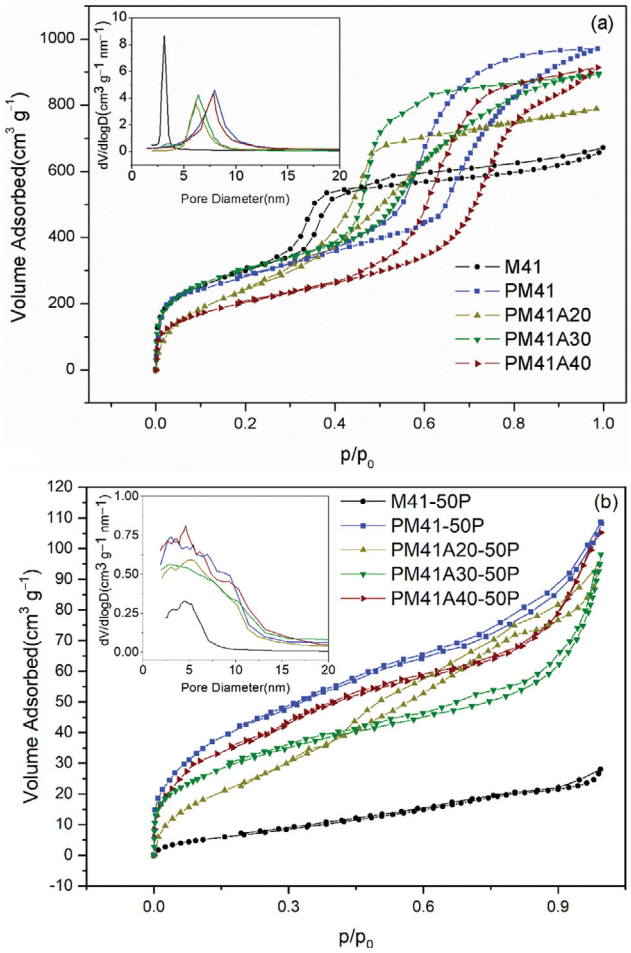

Fig. 2. N_2 isotherms and BJH pore size distributions for (a) M41, PM41, and PM41Ax (x=20, 30, and 40) and (b) M41-50P, PM41-50P, PM41Ax-50P (x=20, 30, and 40).

Table 1. Si/Al atomic ratio and textural parameters characterized by XRF, SXRD, and N_2 isotherms

Support	XRF	SXRD		N_2 adsorption		
	Si/Al[a]	d_{100}[b], nm	a_0[c], nm	S_{BET}[d], $m^2\ g^{-1}$	d_{BJH}[e], nm	V_P[f], $cm^3\ g^{-1}$
M41	-	4.31	4.98	1,098	3.86	1.03
PM41	-	7.85	9.07	981	7.84	1.51
PM41A20	19.5(20)	6.87	7.94	829	6.54	1.30
PM41A30	28.7(30)	6.95	8.02	959	6.66	1.43
PM41A40	38.2(40)	7.65	8.83	971	7.60	1.45
M41-50P	-	-	-	19	-	0.11
PM41-50P	-	-	-	127	-	0.32
PM41A20-50P	-	-	-	106	-	0.26
PM41A30-50P	-	-	-	134	-	0.39
PM41A40-50P	-	-	-	125	-	0.31

[a]Si/Al atomic ratio measured by XRF.
[b]Basal spacing obtained from SXRD.
[c]Unit cell calculated by the equation: $a_0 = \frac{2d_{100}}{\sqrt{3}}$.
[d]Specific surface area determined from the adsorption branch in a relative pressure range of p/p_0=0.05-0.3 by BET method.
[e]Pore diameter fixed by BJH method.
[f]Pore volume corresponding to the N_2 amount adsorbed at a relative pressure of ca. 0.99.

In the range of p/p_0=0.3–0.4, M41 is characterized by comparatively steep capillary condensation and evaporation steps, as well as pronounced inflexions at both ends, suggestive of narrowly distributed mesopores [65]. Moreover, we can observe a hybrid hysteresis loop of types H1 and H4. After pore expansion, all capillary behavior starts at a higher relative pressure, e.g., p/p_0=0.45 for PM41A20 and PM41A30, and 0.6 for PM41 and PM41Al40, confirming the occurrence of larger pores, as seen in Table 1. The strikingly magnified hysteresis areas are relevant with the expanded pores, i.e., when the pore size is larger than 4 nm, the asynchrony of capillary condensation and evaporation is more remarkable [56]. Furthermore, Fig. 2(a) shows an extensively distributed pore size after pore expansion, which agrees well with the broader and gentler capillary condensation steps [66]. These variations demonstrate that the pore expansion is accompanied by structural deterioration [65].

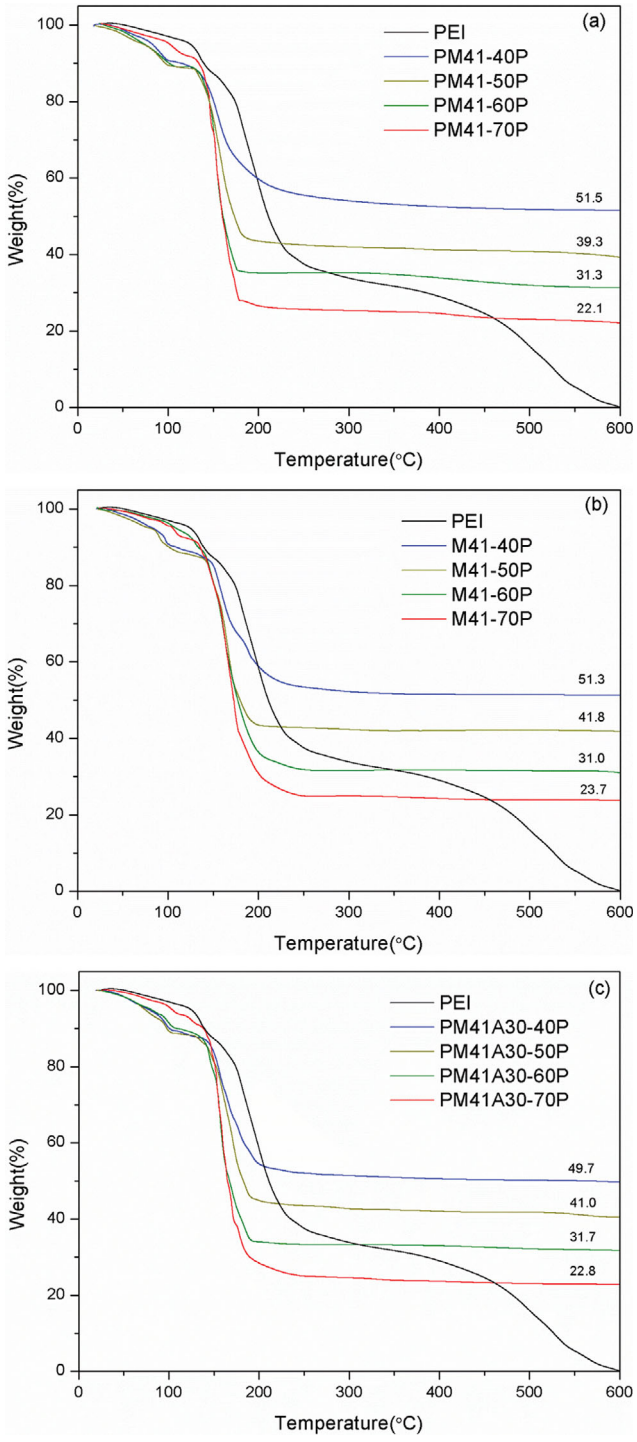

Fig. 3. TGA profiles for (a) PEI and PM41-yP, (b) PEI and M41-yP, and (c) PEI and PM41A30-yP (y=40, 50, 60, and 70).

When 50 wt% of PEI is loaded, all V_P and S_{BET} sharply decreased because of PEI filling the pore volume [27], which gave rise to a similar type-II isotherm (Fig. 2(b)).

Fig. 3(a) shows the TGA profiles of pure bulk PEI and PM41-yP (y=40, 50, 60, and 70). Regarding pure bulk PEI, it lost ~3.0% of initial weight at 100 °C, which was attributed to the desorption of pre-absorbed moisture and CO_2. A notable weight loss occurred between 150 and 225 °C. Then, the decomposition slowed and came to completion at 600 °C, implying that 600 °C is sufficient to determine the amount of PEI loading. In the literature, similar thermo-decomposition processes for pure bulk PEI are available [27].

When the PEI loading was <60 wt%, all samples showed ~10% weight loss at 100 °C, which was attributed to pre-absorbed moisture and CO_2 removal. As the temperature increased, a considerable weight loss occurred between 130 and 170 °C. The weight loss was lower and more narrowly distributed than that of pure bulk PEI, illustrating that PEI was uniformly dispersed within the nano-sized pores forming smaller particles. Finally, the total weight loss was 48.5, 60.7, and 68.7 wt%. When the pre-absorbed species were excluded from the total weight of the sample, the actual PEI loading rates were close to the designed value. For 70 wt% PEI loading, similar to that of pure bulk PEI, the weight loss decreased to ~4.5 wt% at 100 °C. This phenomenon indicates that PEI was coated on the external surface of PM41; thus, it behaved similarly to pure bulk PEI. Moreover, the PEI coating outside, hereafter denoted as PEI coating, wrapped the adsorbent as a PEI film, hindering the escape of gas entrapped in the pores. Thus, in the range of 130-170 °C, most PEI and the trapped gas were removed. Finally, the total weight loss was 77.9 wt%, and the actual PEI loading rate was similar to the design value (70 wt%) when ~10% pre-absorbed gas was removed. Previously, similar thermo-decomposition behavior for heavily PEI-loaded samples has been reported [34,67].

Figs. 3(b) and (c) show the TGA curves of M41-yP and PM41A30-yP (y=40, 50, 60, and 70), respectively. For each sample, the actual PEI loading rate obtained from the total weight loss was close to the designed value. In addition, regarding M41-yP, when the PEI loading rate was ≥60 wt%, the thermo-decomposition characteristic within 100 °C behaved similar to that of pure bulk PEI. This illustrates the coating of PEI emerged at a PEI loading of 60 wt% for M41-yP, earlier than that (70 wt%) of PM41-yP and PM41A30-yP. Because the pore shrinkage decreases the maximum PEI loading capacity in the pores, leading to the earlier occurrence of PEI coating for M41. Therefore, the pore size and volume of the support determine the opportunity when the coating of PEI emerges.

Fig. 4 shows the SEM images of M41 loaded with and without 60 wt% PEI, and the PM41A30 counterparts, as well as the EDX

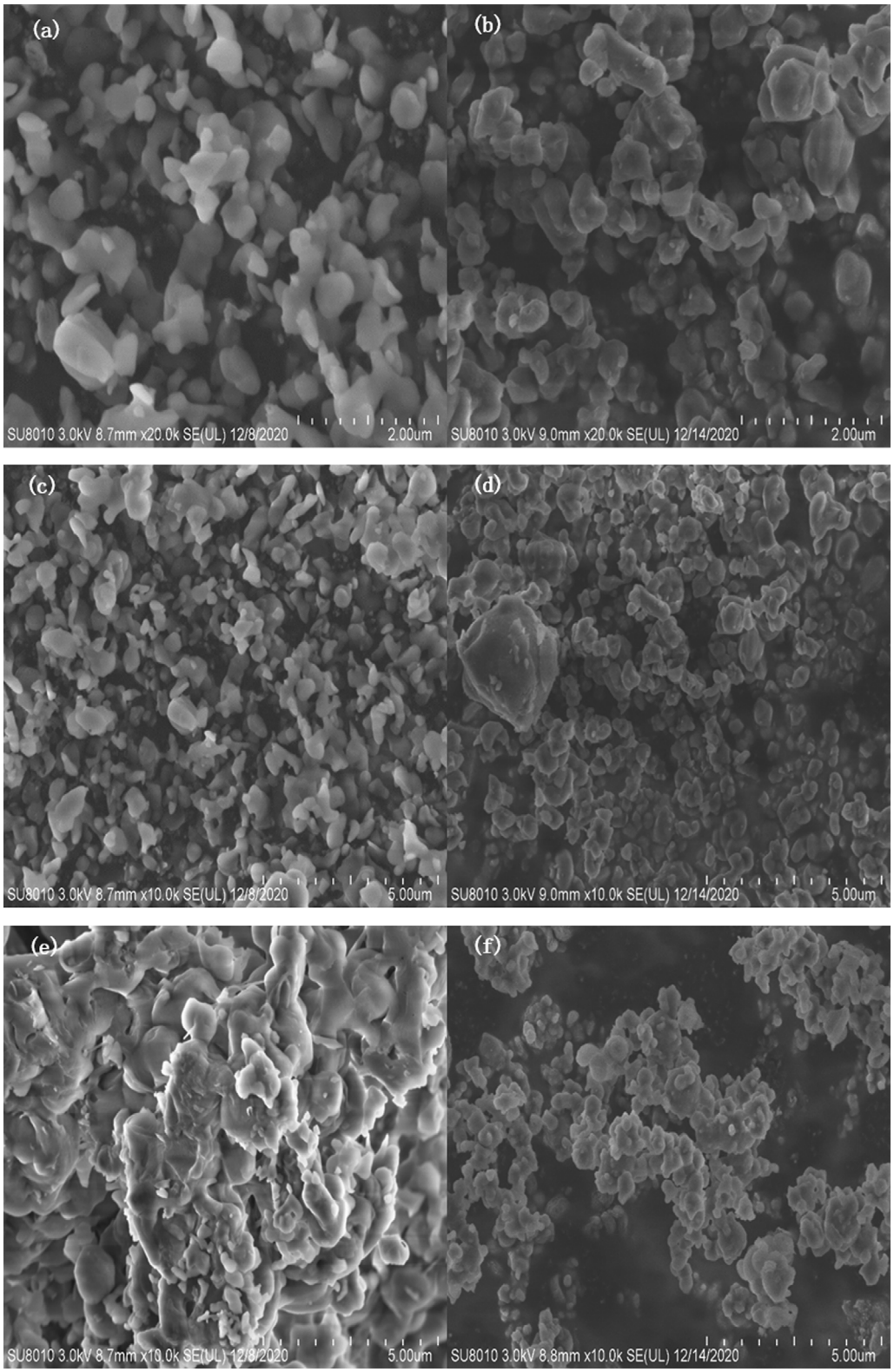

Fig. 4. SEM images of (a) (c) M41, (b) (d) PM41A30, (e) (g) M41-60P, and (f) (h) PM41A30-60P, and energy-dispersive X-ray spectroscopy (EDX) patterns of (i) M41-60P and (j) PM41A30-60P.

patterns of M41-60P and PM41A30-60P. Fig. 4(a)-(d) shows that M41 and PM41Al30, free of PEI, exhibit dispersive block-like morphology. Most observed particles had a smaller size value of <1 μm. For samples loaded with PEI, M41-60P had noticeable agglomeration, while PM41A30-60P did not (Fig. 4(e)-(h)). Wang et al. reported that at 60 wt% PEI loading, the PEI coating emerged for

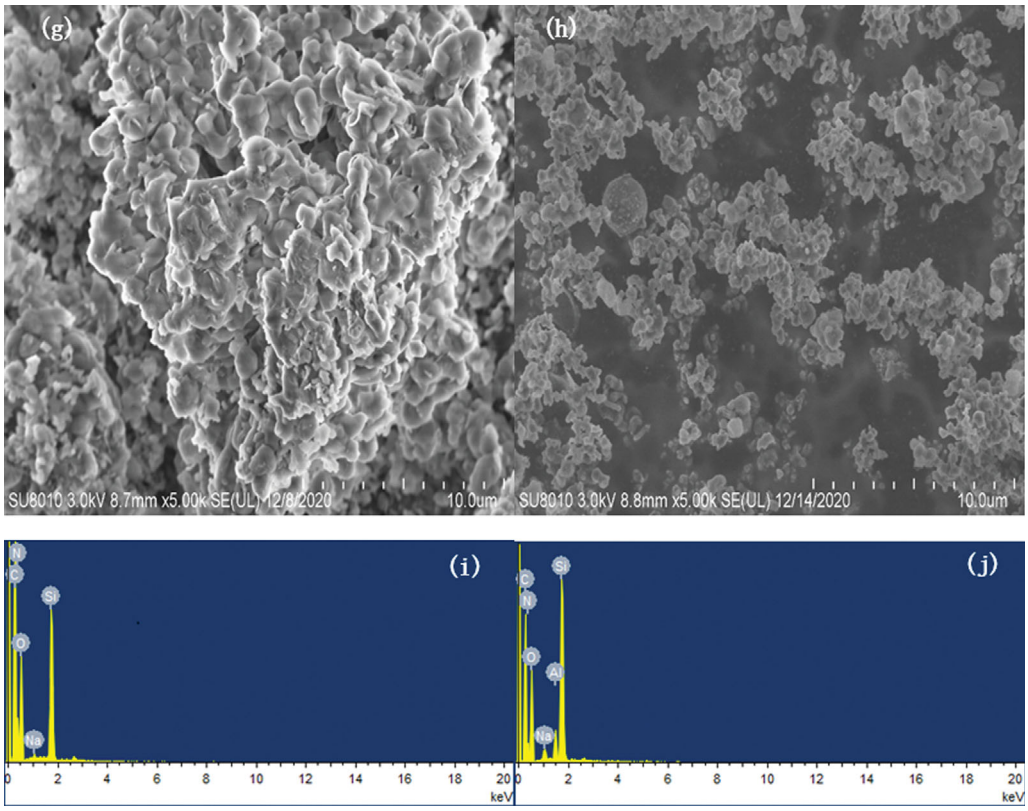

Fig. 4. Continued.

M41-60P such that sticky PEI agglomerated the dispersive M41-60P particles [57]. For PM41A30-60P, its particles still retained comparably better independence with each other because of the capacity of holding all PEI in the pores, which agrees with the abovementioned TGA analysis. As a confirmation of the occurrence of PEI, we presented the EDX patterns of M41-60P and PM41A30-60P. As expected, a noticeable N-peak on the EDX pattern was observed for both [5].

Fig. 5 shows the particle size distribution of (a) M41 and M41-60P and (b) PM41A30 and PM41A30-60P. The mean particle diameter is ~1 μm for both M41 and PM41, which agrees well with SEM results. After loading PEI, both the corresponding particle size increased. Note that the mean particle diameter of M41 was magnified by ~4 times, thus confirming the occurrence of agglomeration.

Fig. 6(a) shows the FTIR patterns of M41, PM41, PM41A20, PM41A30, and PM41A40. From all MCM-41-type supports, we can observe representative vibrations belonging to the tetrahedra

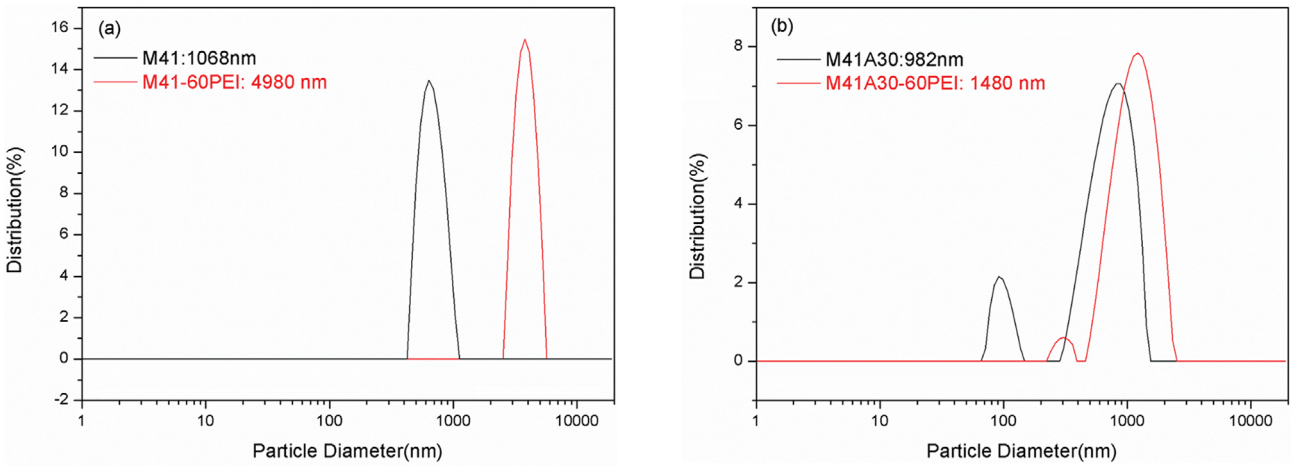

Fig. 5. Particle size distribution of (a) M41 loaded with and without 60 wt% PEI, and (b) PM41A30 loaded with and without 60 wt% PEI.

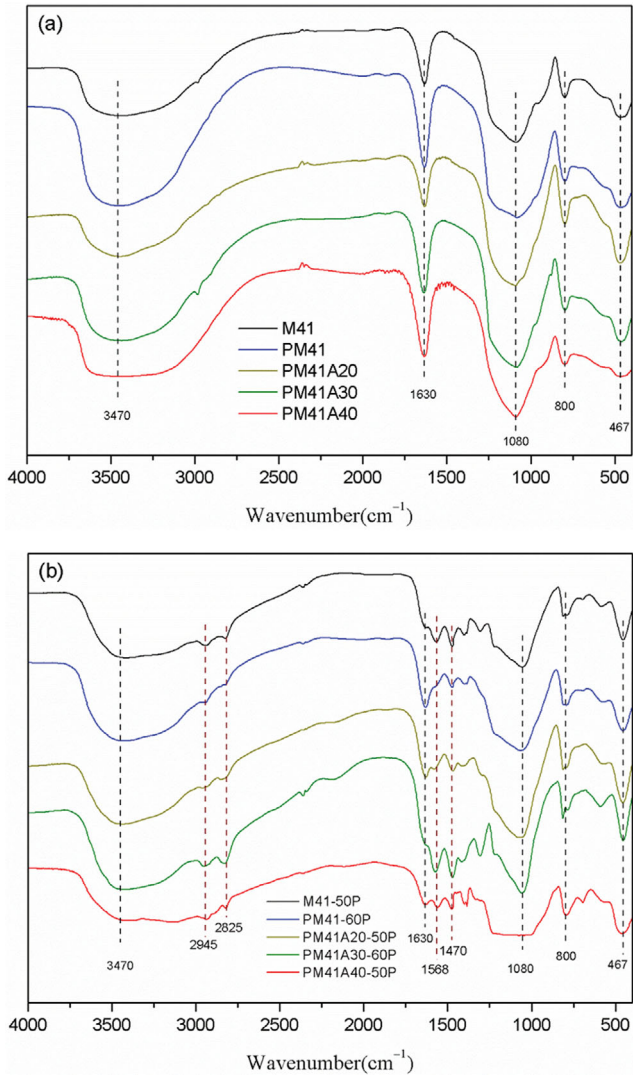

Fig. 6. FTIR patterns for (a) M41, PM41, PM41A20, PM41A30, and PM41A40 and (b) M41-50P, PM41-60P, PM41A20-50P, PM41A30-60P, and PM41A40-50P.

$[SiO_2]_n$ framework, i.e., bands at 1,050, 800, and 467 cm^{-1}, corresponding to the asymmetric and symmetric stretching vibrations and bending vibration of siloxane Si-O-Si, respectively, in addition to the peaks closely related to the adsorbed water and surface silanol Si-OH, namely, bands at 1,630 and 3,470 cm^{-1} [18,19]. When these supports were impregnated by PEI, as shown in Fig. 6(b), we can see exclusive peaks for all resulting samples, which are relevant to the PEI appearance, i.e., bands at 2,945 and 2,825 cm^{-1}, which can be attributed to C-H asymmetric and symmetric stretching vibrations, respectively; at 1,470 cm^{-1} because of the deformation vibration of CH_2, and at 1,568 cm^{-1} owing to the N-H vibration [5,29].

2. CO_2 Adsorption

2-1. Effect of Pore Expansion and Incorporation of Heteroatom Al

Multiple studies [27,33,68] have demonstrated that despite the exothermic nature of CO_2-amine reaction, 75 °C is the most favorable temperature for CO_2 capture concerning high-PEI-loaded (≥40 wt%) MCM-41-type adsorbents. Therefore, in this study, most adsorption experiments were conducted at 75 °C.

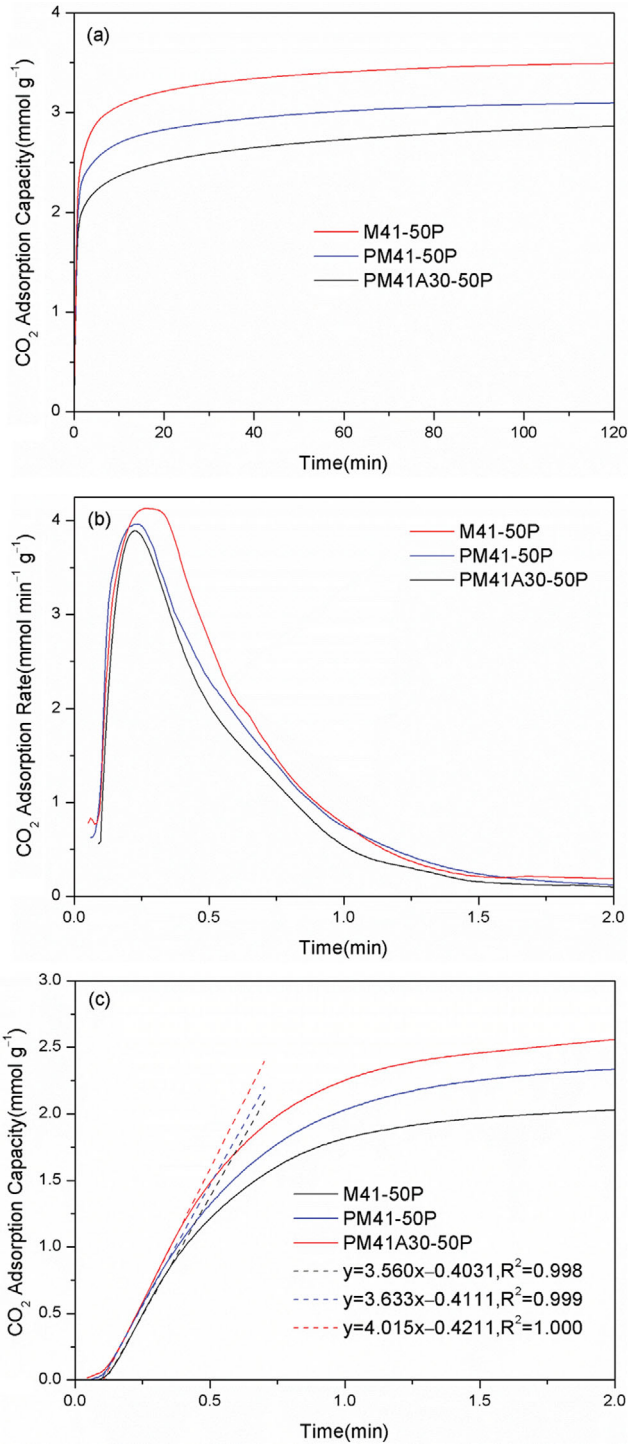

Fig. 7. Time-dependent CO_2 adsorption profiles of M41-50P, PM41-50P, and PM41A30-50P, concerning (a) adsorption capacity in 120 min of the time frame, (b) instantaneous adsorption rate in the first 2 min of contact time, and (c) linearized adsorption rate. Experimental conditions: pure CO_2 stream; temperature=75 °C; flow rate=100 mL min^{-1}; and time duration=120 min.

We present an insight into the effect of pore expansion treatment and incorporation of heteroatom Al on CO_2 adsorption starting from the most frequently used PEI loading rate, i.e. 50 wt%. Fig. 7 shows the time evolution of CO_2 adsorption capacity and adsorption rate for M41-50P, PM41-50P, and PM41Al30-50P on exposure to a pure CO_2 flow at 75 °C. As shown in Fig. 7(a), the equilibrium adsorption capacity of CO_2 followed the order: M41-50P (2.86 mmol g^{-1})<PM41-50P (3.09 mmol g^{-1})<PM41Al30-50P (3.49 mmol g^{-1}). The adsorption capacity of M41-50P was close to but slightly higher than that (2.55 mmol g^{-1}) reported by Xu et al. [27] under the same adsorption conditions. When using PM41, the adsorption capacity increased by 8.1% compared to that of M41-50P. The advantage was attributed to improved CO_2 diffusion within the larger pores and consequently more effective interactions with adsorption sites [25,31]. After Al doping, the adsorption capacity increased further by 12.8% compared to that of PM41-50P. Xu et al. [34] attributed the increased adsorption capacity to the enlarged pore volume after the incorporation of the heteroatom Al. However, this conclusion is unsuitable for the present study because all the pore volumes of framework-substituted supports investigated here (Si/Al=20, 30, and 40) decreased, as clearly seen in Table 1 and reported in previous studies [46,69,70]. As shown in Table 2, PM41A30 has an uptake of 0.78 mmol g^{-1}, which is significantly higher than that of isolated M41 (0.21 mmol g^{-1}) and PM41 (0.28 mmol g^{-1}), respectively. Therefore, when loaded with the same amount of PEI, PM41A30-50P achieves the maximum capacity. Al-containing MCM-41-type materials have many exchangeable cations (e.g., Na^+, K^+, Ca^{2+}, and Mg^{2+}) used for balancing the negative charge created by the substitution of an AlO_4 tetrahedron for a SiO_4 tetrahedron [71]. The resulting metal cations located in the pores throughout the structure showed physisorption over CO_2 through an ion-dipole interaction, which is frequently observed when using zeolites [6]. Consequently, it is the zeolite-like property that improves the CO_2 adsorption capacity for Al-containing MCM-41-type adsorbents. This adsorption via the exchangeable cations throughout the Al-containing MCM-41-type materials is frequently used to remove heavy metals and dyestuff from an aqueous solution [69,70,72]. In this study, this property of Al-containing MCM-41-type materials was innovatively applied to CO_2 capture.

In terms of instantaneous adsorption rate, as shown in Fig. 7(b), all adsorbents exhibited parabola-like profiles of uptake vs. time, which peaked at ~0.25 min, followed by a rapid decline and finally resulting in a slower but steadily decreasing trend after ~1.5 min. Because of the larger pore size and volume, PM41-50P is superior to M41-50P. In addition to larger pore size and pore volume, PM41A30-50P is built on the Al-containing support possessing excellent adsorption performance, thus outperforming its counterparts. As shown in Fig. 7(c), the linearized adsorption rates are 3.56, 3.63, and 4.02 mmol min^{-1} g^{-1}) for M41-50P, PM41-50P, and PM41A30-50P, respectively, which agrees well with the result of instantaneous rates.

2-2. Effect of PEI Loading

Fig. 8 shows the effect of PEI loading rate (40-70 wt%) on CO_2 adsorption capacity, PEI efficiency, and linearized adsorption rate after 120 min of exposure to pure CO_2 stream at 75 °C. As shown in Fig. 8(a), the CO_2 adsorption capacity increased with the PEI loading rate. Generally, the effect of PEI loading rate on adsorption capacity within a finite time framework may be either posi-

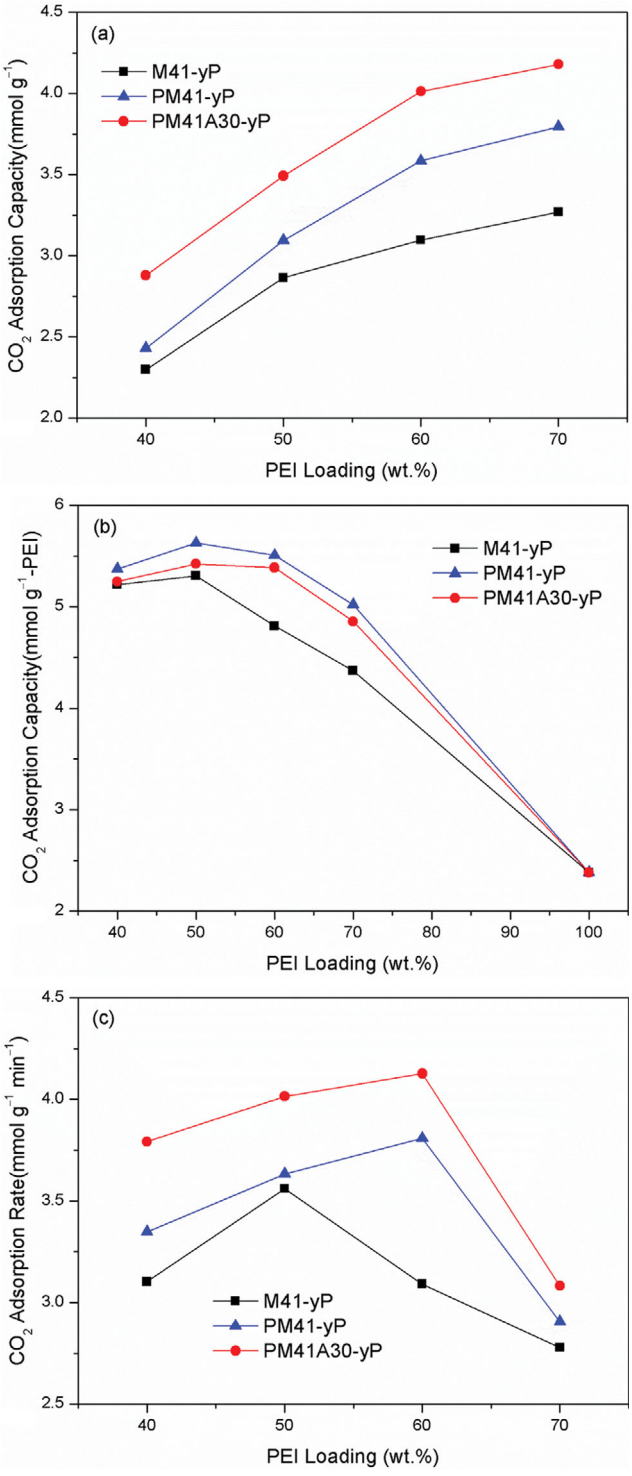

Fig. 8. (a) CO_2 adsorption capacity, (b) PEI efficiency, and (c) linearized adsorption rate for M41, PM41, and PM41A30 impregnated with the PEI loading of 40. 50, 60, and 70 wt%. Experimental conditions: pure CO_2 stream; temperature= 75 °C; flow rate=100 mL min^{-1}; and time duration=120 min.

Table 2. Adsorption capacity, PEI efficiency, and CO_2/N ratio of all samples investigated in this work and fitted straight line for linearized adsorption rate and coefficient of determination (R^2)

Adsorbent (temperature)[a]	Adsorption capacity (mmol g^{-1})	PEI efficiency (mmol g^{-1})	CO_2/N	Fitted line	R^2
Pure PEI (75)	-	2.38	0.105	y=1.581x−0.0325	0.999
M41 only (75)	0.21	-	-	y=0.313x−0.0187	1.000
PM41 only (75)	0.28	-	-	y=0.456x−0.0134	1.000
PM41A20 only (75)	0.95	-	-	y=0.930x−0.0251	0.999
PM41A30 only (75)	0.78	-	-	y=0.878x−0.0208	0.999
PM41A40 only (75)	0.58	-	-	y=0.723x−0.0267	1.000
M41-40P (75)	2.30	5.22	0.230	y=3.103x−0.2864	0.994
M41-50P (75)	2.86	5.31	0.234	y=3.560x−0.4031	0.998
M41-60P (75)	3.10	4.81	0.212	y=3.091x−0.3511	1.000
M41-70P (75)	3.27	4.37	0.193	y=2.778x−0.4001	0.999
PM41-40P (75)	2.43	5.37	0.237	y=3.348x−0.1802	0.996
PM41-50P (75)	3.09	5.63	0.248	y=3.633x−0.3505	0.999
PM41-60P (75)	3.58	5.51	0.243	y=3.808x−0.4111	0.999
PM41-70P (75)	3.80	5.02	0.221	y=2.905x−0.3926	1.000
PM41A20-50P (75)	3.57	5.18	0.228	y=4.163x−0.4275	1.000
PM41A20-70P (75)	4.05	4.39	0.193	y=2.982x−0.4733	1.000
PM41A30-40P (75)	2.88	5.25	0.231	y=3.792x−0.3153	0.999
PM41A30-50P (75)	3.49	5.42	0.239	y=4.015x−0.4211	1.000
PM41A30-60P (25)	2.80	3.36	0.148	y=0.516x−0.0621	1.000
PM41A30-60P (50)	3.08	3.83	0.169	y=1.370x−0.1499	1.000
PM41A30-60P (75)	4.01	5.39	0.237	y=4.127x−0.4626	1.000
PM41A30-60P (100)	3.24	4.10	0.180	y=4.438x−0.3802	1.000
PM41A30-70P (75)	4.18	4.86	0.214	y=3.082x−0.4136	1.000
PM41A40-50P (75)	3.31	5.46	0.240	y=3.793x−0.4240	0.999
PM41A40-70P (75)	4.01	4.91	0.216	y=2.937x−0.3933	1.000

tive or negative [73,74]. Regarding PEI-loaded solids, the diffusional resistance for CO_2 always increases with the number of adsorption sites. Thus, the final adsorption capacity is determined by the interplay between two mutually restricted factors: increased diffusional resistance and an increasing number of adsorption sites. Because of the excellent molecule mobility at 75 °C, uptake is more strongly dependent on the number of adsorption sites than on the mass transfer resistance, resulting in a positive correlation with PEI loading, consistent with previous studies [27,48,73]. Furthermore, as shown in Fig. 8, the positive impact of pore expansion treatment and the incorporation of heteroatom Al on CO_2 adsorption capacity at 50 wt% PEI loading, as shown in Section 3.2.1, is applicable to other PEI loading rates investigated in this study: M41-yP<PM41-yP<PM41A30-yP (y=40, 50, 60 and 70).

Significantly, by comparing the profiles of PM41-yP and M41-yP in Fig. 8(a), as the PEI loading rate increased from 50 to 60 wt%, the uptake increment resulting from the pore expansion treatment was magnified. This phenomenon is associated with the variation of PEI efficiency with PEI loading. Fig. 8(b) shows that the PEI efficiency of PM41-yP is slightly higher than that of M41-yP at a PEI loading of <50 wt%. Thus, as per Eq. (1), PM41-yP has a somewhat larger adsorption capacity than M41-yP. With an additional increase in PEI loading to 60 wt%, the PEI efficiency of M41-60P sharply declined while PM41-60P remained at a relatively high level. Consequently, the magnified increment in PEI efficiency at 60 wt% PEI loading resulted in a remarkable increment in CO_2 adsorption capacity at PEI loading of >50 wt%.

As per Xu et al. [27], the noticeable difference in PEI efficiency between M41-yP and PM41-yP at 60 wt% PEI loading can be explained. In particular, in this study. the pore volume of M41 used was ~1.03 cm^3 g^{-1}, and the density of PEI was ~1 g cm^{-3}. Thus, the theoretically maximum internal PEI loading capacity is ~1 g-PEI g^{-1}-M41, i.e., 50 wt% PEI loading. In this case, the adsorption of CO_2 by PEI is greatly enhanced because of a synergistic interaction between PEI and M41 [27]. The PEI particles are completely expanded and homogeneously scattered on the high surface of M41, making them easily accessible. As a confirmation of this phenomenon, Table 2 shows the uptake of pure PEI, ~2.380 mmol-CO_2 g^{-1}-PEI, is only 44.9% of that of M41-50P. As shown by TGA curves in Fig. 3(b), once the PEI loading rate exceeded 50 wt%, e.g. 60 wt%, the internal porous volume of M41 could no longer store all of the PEI, and the excess had to be coated on the exterior surface. As the PEI loading rate increased from 50 to 60 wt%, covered PEI results in a substantial decreased in PEI efficiency for M41. However, for PM41 with a pore volume of 1.51 cm^3 g^{-1}, the case is different. Its theoretically maximum internal PEI loading capacity increased to 1.5 g-PEI g^{-1}-PM41, indicating no PEI coating occurred at 60 wt% PEI loading, thus preserving a relatively

high PEI efficiency (5.51 mmol g^{-1}-PEI). Consequently, PM41 can accommodate more PEI within its pores than M41, resulting in a significant improvement in PEI efficiency and CO_2 adsorption capacity under heavy PEI loading.

The pore volume of the PM41A30 support (1.43 cm^3 g^{-1}) is similar to that of PM41. Thus, the curve of PEI efficiency versus PEI loading is comparable to that of PM41, as clearly seen in Fig. 8(b), i.e., maintaining relatively high PEI efficiency at a PEI loading of ≤60 wt%, followed by a visible decline in PEI efficiency above this loading. However, the PEI efficiency of PM41A30-yP is slightly lower than that of PM41-yP at the same PEI loading, which is probably attributable to the adsorption competition with the exchangeable cations in the pores of Al-containing adsorbents. However, in terms of adsorption capacity, PM41A30-yP still outperforms PM41-yP because of its remarkable superiority due to the Al-containing self-support.

In terms of the stoichiometric ratio of CO_2 and amine (CO_2/N), i.e., moles of CO_2 adsorbed per mole of amine, the values of CO_2/N generally increased after pore expansion, particularly when the PEI loading exceeded 50 wt%, further demonstrating the influence of pore expansion on CO_2 adsorption. The maximum ratio of CO_2/N (0.248) in this study was obtained when PM41-50P was used, which is still well below the theoretical maximum of 0.5; however, it is higher than that of M41-supported PEI [27,48,68].

Identically, the dependence of the CO_2 adsorption rate on PEI loading is closely related to the maximum internal PEI loading capacity. As shown in Fig. 8(c), the linearized adsorption rate started decreasing after the internal pore volume was occupied by PEI, i.e., 50 wt% for M41-yP versus 60 wt% for PM41-yP. With the appearance of PEI coating, the resulting PEI-film slowed the interaction between CO_2 and internal active sites. In addition to the intrinsically slow rate by pure PEI, the final adsorption rate drastically decreased. Similar behavior was reported by Xu et al. [34] wherein the linearized adsorption rate by M41-50P was much faster than that of M41-75P.

2-3. Effect of Si/Al

Fig. 9 shows (a) the CO_2 adsorption capacity and (b) PEI efficiency as a function of the Si/Al ratio at 50 wt% and 70 wt% PEI loadings upon 120 min of exposure to a pure CO_2 stream at 75 °C. As shown in Fig. 9(a), at 50 wt% PEI loading, the CO_2 adsorption capacity decreased with an increasing Si/Al ratio because of the lower Si/Al ratio and the higher CO_2 uptake of the support self,

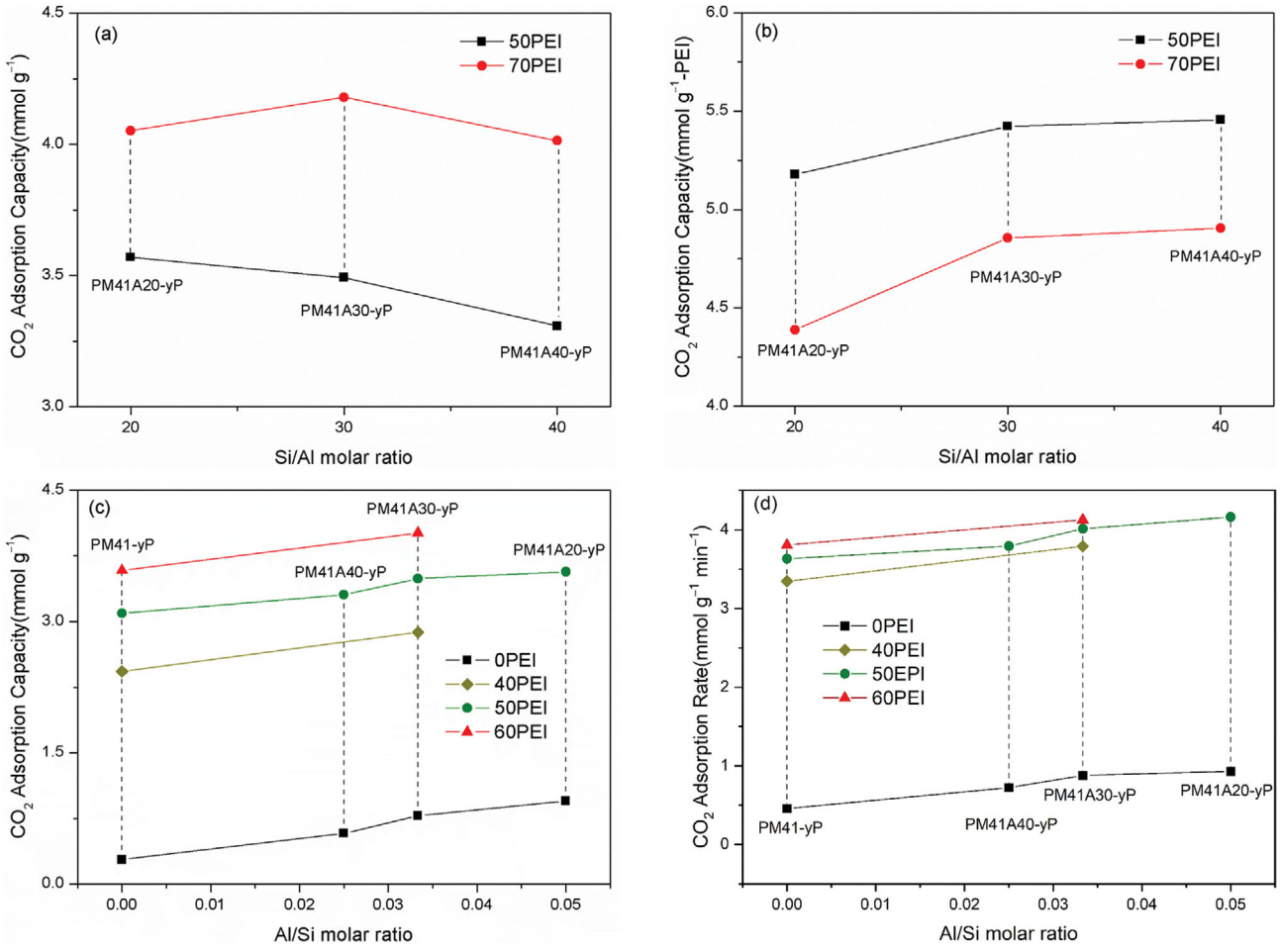

Fig. 9. (a) CO_2 adsorption capacity and (b) PEI efficiency for the adsorbents with different Si/Al molar ratios and summary of (c) CO_2 adsorption capacity and (d) linearized adsorption rate at a PEI loading of <70 wt%. Experimental conditions: pure CO_2 stream; temperature= 75 °C; flow rate=100 mL min^{-1}; and time duration=120 min.

thus resulting in the higher CO_2 uptake of the resultant adsorbent (Table 2). However, at 70 wt% PEI loading, the CO_2 adsorption capacity exhibited a non-monotonic trend as the Si/Al ratio increased. It is easily understood that the superior adsorption capacity of PM41A30-70P compared to PM41A40-70P is attributable to its high Al-containing support possessing a higher adsorption performance. Surprisingly, despite Si/Al dropping from 30 to 20, the adsorption capacity did not increase with an additional increase in Al content. This behavior can be explained by the fact that, as seen in Fig. 9(b), the PEI efficiency simultaneously decreased with Si/Al dropping from 30 to 20, i.e., the adsorption increment obtained from high Al-content support cannot compensate for the loss in PEI efficiency. Therefore, PM41A20-70P, although built on highly functional support, exhibited a remarkably lower adsorption capacity than PM41A30-70P.

In terms of the effect of the Si/Al molar ratio on PEI efficiency, for 50 wt% PEI loading, the PEI efficiency increased marginally as the Si/Al ratio increased, and this minor increment is associated with the decreased adsorption competition with less heteroatom Al. Hence, for the different Si/Al ratios of adsorbents at 50 wt% PEI loading, the uptake by the support self, other than PEI efficiency, is the predominant factor in determining the CO_2 adsorption capacity. At 70 wt% PEI loading, with the appearance of the PEI coating, PEI efficiency sharply decreased compared to that at 50 wt% while maintaining the Si/Al molar ratio constant. As the Si/Al ratio increased from 20 to 30, the PEI efficiency did not show a slight increase, as it did at 50 wt% PEI loading, but rather presented a marked increase. This phenomenon is attributable to the increased support pore volume (from 1.30 to 1.43 $m^3\ g^{-1}$) as the Si/Al ratio varied from 20 to 30, which can be seen in Table 1. There was more PEI coating for PM41A20-70P than for PM41A30-70P, which resulted in a marked increment in PEI efficiency as the Si/Al ratio increased from 20 to 30. The noticeable decrease in the pore volume of Al-containing pore-expanded MCM-41 occurred when Si/Al molar ratio was 30, as reported by Hessam et al. [56]. Hence, the result is reproducible. With an additional increase in the Si/Al ratio from 30 to 40, the PEI efficiency slightly increased, similar to the situation at 50 wt% PEI loading. The support volume did not show significant variation (1.45 vs. 1.43 $cm^3\ g^{-1}$) during this process. Therefore, PEI efficiency depends on the Si/Al ratio in the support other than the amount of PEI coating. Thus, the combination of the Si/Al molar ratio and PEI efficiency determines adsorption capacity at 70 wt% PEI loading.

As confirmed above, at 70 wt% PEI loading, the adsorption capacity was dependent on the Al content of the support as well as the PEI efficiency. To confirm the increased adsorption capacity of the Al-containing adsorbent obtained from its self-support, we combined all the pore-expanded adsorbents except that at 70 wt% PEI loading for comparison, which is displayed in Fig. 9(c). The CO_2 adsorption capacity on the self-support increased as the Al/Si ratio increased from 0 to 0.05, i.e., over the entire Al/Si range investigated in this study, being 0.28, 0.58, 0.78, and 0.95 mmol g^{-1} for PM41, PM41A40, PM41A30, and PM41A20, respectively. An almost synchronous increase in adsorption capacity was observed for 50 wt% PEI loading, as the adsorption curve of 0 PEI was almost parallel with that of 50 PEI, illustrating that the incorporated Al positively influenced the adsorption capacity of the corresponding adsorbent. For the PEI loading at 40 and 60 wt%, despite Al/Si changing in a local range, we witnessed the synchronous increase

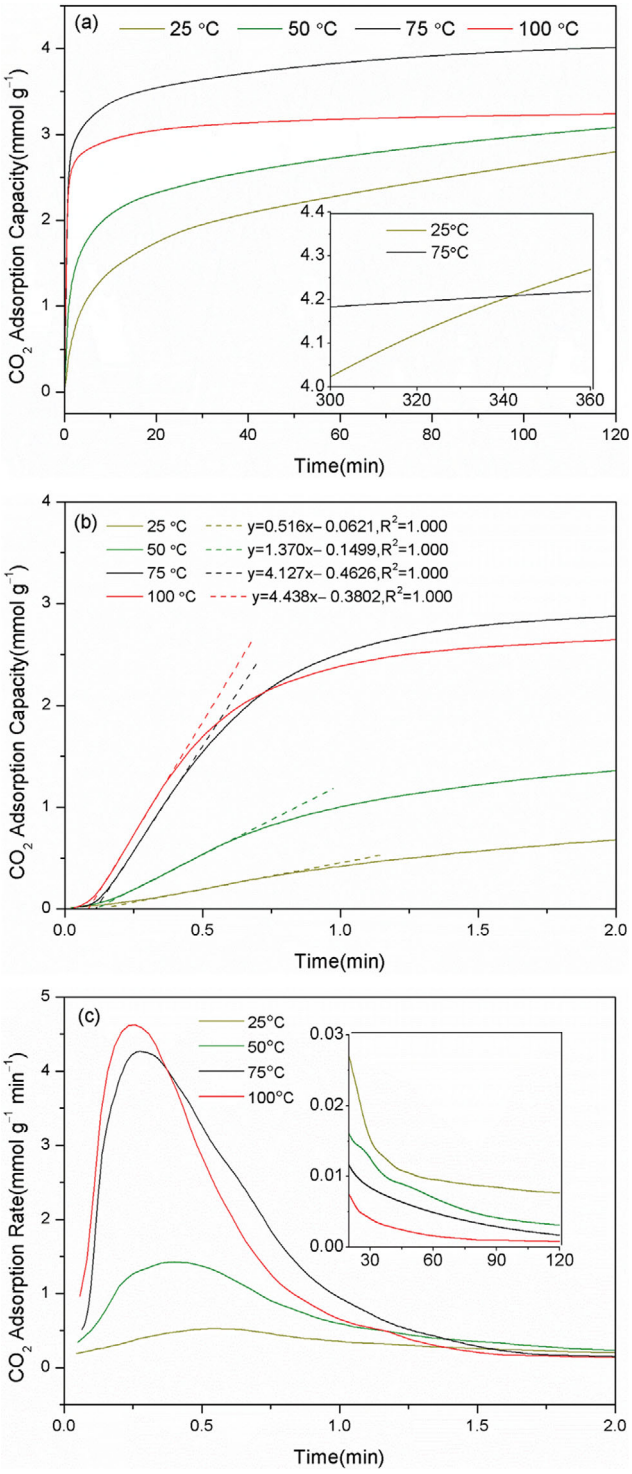

Fig. 10. Time evolution of PM41A30-60P from the aspect of (a) adsorption capacity, (b) linearized adsorption rate, and (c) instantaneous adsorption rate. Experimental conditions: pure CO_2 stream; flow rate=100 mL min^{-1}; adsorption temperature=25, 50, 75, and 100 °C; and time duration=120 min.

in adsorption capacity. Therefore, from the phenomenological point of view, the increase in adsorption capacity was enhanced by incorporating Al, with the increment dependent on the amount of incorporated Al.

As clearly seen in Fig. 9(d), the positive effect of incorporated Al is suitable for the adsorption rate. Furthermore, as the content of incorporated Al increased, samples loaded with and without PEI demonstrated a synchronous increment in the adsorption rate, illustrating that the variation of adsorption rate is relevant to the incorporated Al.

2-4. Temperature Dependence

PM41A30-60P was the best-performing adsorbent investigated in this study. Hence, we used it to investigate the temperature dependence of adsorption. Fig. 10 shows the adsorption capacity and adsorption rate as a function of time at four different temperatures. As seen in Fig. 10(a), within the time frame of 120 min, the adsorption capacity peaked at 75 °C, which was previously reported when using PEI-impregnated MCM-41-type adsorbents [27,30,33, 73,74]. Although low temperatures are favorable thermodynamically, a high temperature facilitates the interaction of CO_2 with additional active sites because of the enhanced mass transfer rate. Therefore, there must be an intermediate temperature to obtain the maximum capacity; regarding PEI-impregnated MCM-41-type adsorbents, 75 °C is the verified optimal temperature for CO_2 capture.

Subsequently, as shown in Fig. 10(b), the linearized adsorption rate increased as the temperature increased. This phenomenon is attributable to the increased mobility of CO_2 molecules, which enables faster access to active sites. As the temperature decreased from 75 to 25 °C, the variation rate was striking, reaching as high as 87%. Serna et al. [23] examined the temperature dependence of CO_2 capture kinetics using PM41-supported TRI and PEI, respectively. They discovered that, as the temperature decreased from 70 to 20 °C, PEI-loaded PM41 showed a much remarkable decrease in kinetics rate constant than its TRI counterparts (93% versus 16%). The sharply decreased adsorption rate with a decrease in temperature is relevant to the nature of PEI. In particular, PEI, a viscous macromolecule dispersed inside the pores, always tends to agglomerate. As more PEI is loaded, the resulting agglomerations significantly increase, which reduces the available space in the channels and restricts the diffusion of CO_2 [23,74]. The magnified diffusion resistance can be counterbalanced by increased mobility at relatively high temperatures, e.g. 75 °C, or else, part of the active sites will become inaccessible [75].

Fig. 10(c) shows the instantaneous adsorption rate at different adsorption temperature. First, we observed a positive temperature dependency, and the variation amplitude with respect to temperature was in line with the linearized rate presented. Next, for a fast adsorption process, the most rapid adsorption stage should concentrate on the head several minutes of contact time, followed by a much slower one with the rate close to zero [24,25,39]. However, this was not the case for the adsorption at 25 °C. Thus, the advantage in the adsorption rate obtained at the initial period was far less evident than that at higher temperatures. This phenomenon is ascribed to the so-called "superposition effect" illustrated above, i.e. the already enhanced diffusion resistance seemed to be amplified further when the molecule movement was inactive at low temperatures.

Furthermore, for subsequent adsorption, it signifies that the inactivity of initial adsorption would reserve additional unoccupied active sites. As confirmed from Fig. 10(c), in the time interval from 20 to 120 min, the instantaneous adsorption rate at 25 °C was faster than others. Therefore, provided the adsorption duration is sufficient, the adsorption capacity at 25 °C may exceed that at 75 °C. This is confirmed from Fig. 10(a), wherein the breakthrough occurs at ~350 min, confirming the exothermic characteristic of the process and verifying the diffusion-controlled type adsorption process at low temperature [23,73].

2-5. Effect of Water Vapor on Adsorption Performance

Water vapor is unavoidable when capturing CO_2 in the post-combustion scenario. To evaluate the effect of water vapor on the adsorption performance, the two-component adsorption apparatus as shown in Fig. 11(a) was employed. The experiment process was as described by Harlick et al. [25]. Typically, ~1 g of PM41A30-60P was packed in the adsorption column. The sample was activated for 1 h at 105 °C under flowing dry N_2 with a flow rate of 100 mL min^{-1}. It was then cooled to 75 °C, and a flow of wet N_2 was introduced at a flow rate of 100 mL min^{-1}. The relative humidity (RH), detected by the RH transmitter, was controlled at 10 and

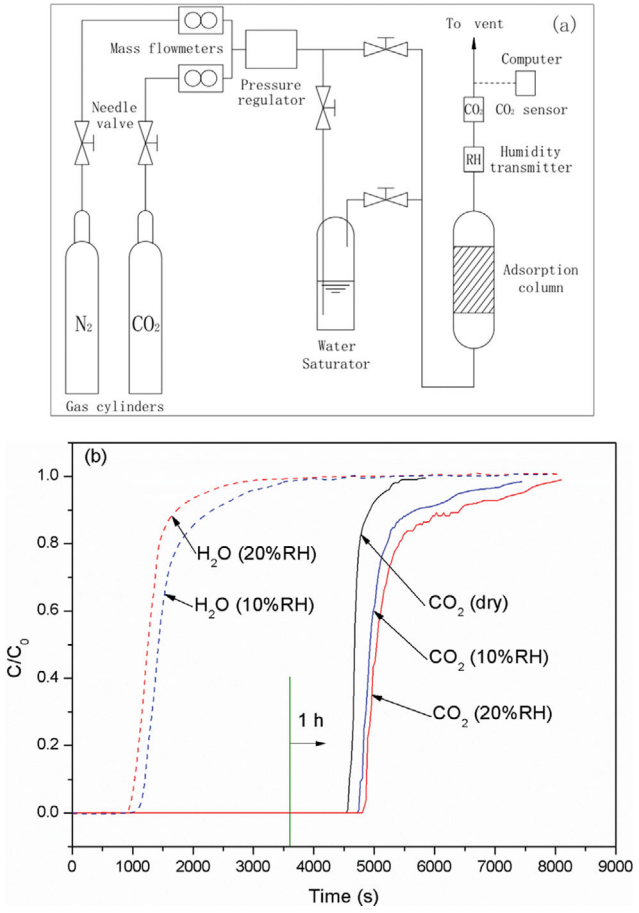

Fig. 11. (a) Schematic diagram of the adsorption apparatus and (b) Breakthrough curves for a CO_2 and N_2 mixture at 75 °C and 1 bar with and without water vapor.

20% by adjusting the temperature of the water saturator to ~28 and 40 °C, respectively. After 1 h, the N_2 source was switched to 5 vol% CO_2/N_2 at the same RH. When the downstream CO_2 concentration, detected by the CO_2 sensor, reached 95% of the feed one, it indicated the completed breakthrough of CO_2. The adsorption of dry 5 vol% CO_2/N_2 was also examined. After the activation of the adsorbent, the dry gas mixture (100 mL min^{-1}) was directly supplied to the column. For a better comparison, its breakthrough curve was moved backward for 1 h.

Fig. 11(b) shows the breakthrough curves. The breakthrough time for water vapor was 47.8 and 36.5 min, and the amount of water vapor adsorbed was 2.81 and 4.51 mmol g^{-1} for 10% and 20% RH, respectively. After 1 h, the adsorption of CO_2 began, using 47.5 and 64 min to complete the breakthrough for 10 and 20% RH, respectively, which was ~2 and 3 times that (26 min) of dry 5 vol% CO_2/Ar. However, the CO_2 adsorption capacity was 25.7 and 36.3% higher than that (2.63 mmol g^{-1}) under dry conditions. The presence of water vapor leads to the partial formation of bicarbonate (RNH_3^+ HCO_3^-) between amine and CO_2, which consumes one amine less than carbamate ($RNHCO_2^-RNH_3^+$) formed under dry conditions [76,77].

3. Adsorption Kinetic Analysis

3-1. Apparent Kinetic Models

Because of the highly fitted similarity among all adsorbents used in this study at 75 °C, we only considered the PM41A30-60P representative to interpret the fit. Fig. 12 shows the experimental data and its fitting profiles to the kinetic models used in this study. The pseudo-first-order and pseudo-second-order models revealed similar trends fitting to the experimental data, i.e., consecutive two times of pre-overestimation and post-underestimation. In terms of fitting accuracy, the pseudo-second-order model is superior, as evidenced by its proximity to the experimental data and a higher value of R^2 compared to the pseudo-first-order model (0.859 vs. 0.601). Its comparatively better fit was attributed to the agreement between its establishment on the assumption of chemical adsorption and the chemically dominated capture of CO_2 by PEI [78]. By contrast, the pseudo-first-order model is more suitable for describing physisorption, which plays a secondary role in adsorption in this study and exhibits more remarkable deviations from experimental data. However, it outperforms the pseudo-second-order model at the initial stages of contact time because of its high suitability for the adsorption process characterized by a relatively low surface coverage [23,39,78].

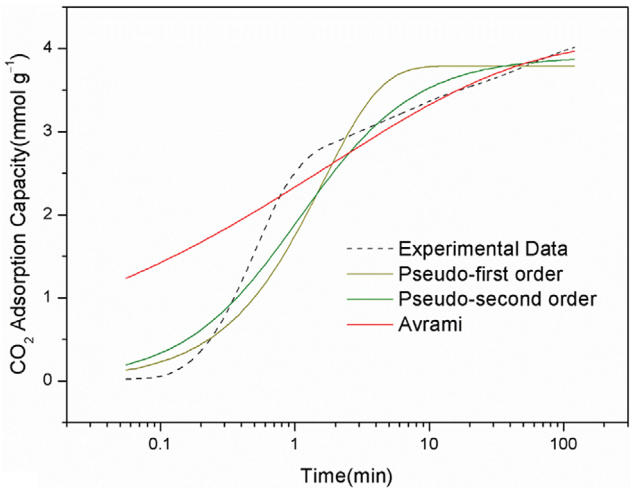

Fig. 12. Experimental data and its fits to kinetic models for PM41A30-60P. Experimental conditions: pure CO_2 stream; flow rate= 100 mL min^{-1}; adsorption temperature=75 °C; and time duration=120 min.

Avrami's fractional-order model exhibited significant deviation from experimental data in the first tens of seconds of contact time, after which it afforded the best fit until the equilibrium stage. The overall fit is controlled within a satisfactory degree of accuracy based on the minimum observed curve deviation after the initial contact period and the highest R^2 value of 0.941. Avrami's fractional-order model simultaneously considers multiple reaction mechanisms involved in a single adsorption process, thus being more suitable for describing the hybrid adsorption process presented in this study, consistent with that reported in the literature [23,28,39,62,78,79]. The fitting process by Avrami's fractional-order model is highly consistent with the report of literature [23] in which PEI-impregnated PM41 was used to capture CO_2.

The experimental data comprises an initial fast adsorption stage followed by a much slower adsorption stage, as presented in the literature [68]. In the first stage, PM41A30-60P demonstrated an exceedingly fast adsorption rate, achieving an uptake of 62.6% of its total capacity within the first few minutes of contact time. The linearized adsorption rate was as high as 4.127 mmol min^{-1} g^{-1}. This favorable adsorption behavior in the initial period of contact time is common among numerous MCM-41-type adsorbents, such as PEI [27,34,48,80], DEA [32], and TRI [23,25]. The adsorption conditions created by MCM-41-type materials, such as fully extended contact surface, homogeneously distributed active sites, reduced diffusion resistance, and promoted mass transfer rate, facilitate an unhindered, fast, and appropriate reaction between CO_2 and active sites.

However, the second stage shows a moderate but steady increase in uptake until the end of the process. The long-tail phenomenon is frequently witnessed in the thermogravimetric adsorption curve for the PEI-loaded adsorbents [75]. Section 3.2.4 has interpreted the distinctly diminished adsorption rate at low temperatures associated with PEI's nature. Additionally, it can explain the quasi-equilibrium of the second stage of adsorption. In particular, PEI is uniformly dispersed within the channels of MCM-41-type materials as bulk viscous agglomerations, resulting in a large number of adsorption sites involving exposed and covered amine groups. The exposed branched amines are easily accessible for CO_2 at 75 °C because of the synergistic effect produced by MCM-41-type materials [27,34], resulting in fast adsorption. After depleting the exposed amines, the covered amines begin to dominate the following adsorption, leading to a considerable decrease in the subsequent adsorption rate because of significantly enhanced diffusional resistance [23,27,34,74,80]. Avrami's exponent n_A, reflecting the growth dimensions of adsorption sites, is only 0.290, illustrating that with the deepening of reaction, the accessibility of unoccupied active sites becomes more difficult. However, for Avrami's rate constant k_A= 0.579 min^{-1}, the overall adsorption process is comparatively fast.

Table 3. Kinetic rate constants, characteristic parameters, and coefficient of regression (R^2) for all adsorbents investigated in this study

PEI (wt%) [Temp. (°C)]	Pseudo-first order			Pseudo-second order			Avrami's fractional order			
	q_e mmol g^{-1}	k_1 min^{-1}	R^2	q_e mmol g^{-1}	k_2 g $mmol^{-1}$ min^{-1}	R^2	q_e mmol g^{-1}	K_A min^{-1}	n_A	R^2
M41 for adsorption										
40[75]	2.19	0.718	0.595	2.25	0.496	0.875	2.32	0.765	0.303	0.948
50[75]	2.69	0.609	0.552	2.78	0.324	0.841	2.97	0.510	0.276	0.948
60[75]	2.88	0.316	0.556	3.01	0.167	0.844	3.43	0.175	0.275	0.975
70[75]	3.01	0.184	0.654	3.20	0.096	0.888	3.67	0.097	0.314	0.988
PM41 for adsorption										
40 [75]	2.33	0.968	0.618	2.38	0.633	0.882	2.44	1.135	0.300	0.945
50 [75]	2.97	0.742	0.666	3.05	0.387	0.904	3.10	0.803	0.335	0.934
60 [75]	3.44	0.708	0.664	3.53	0.316	0.906	3.60	0.747	0.339	0.938
70 [75]	3.53	0.312	0.672	3.69	0.137	0.903	3.92	0.250	0.330	0.968
PM41A20 for adsorption										
50 [75]	3.40	0.708	0.623	3.49	0.316	0.882	3.60	0.733	0.307	0.947
70 [75]	3.74	0.245	0.631	3.94	0.101	0.878	4.40	0.145	0.308	0.976
PM41A30 for adsorption										
40 [75]	2.76	1.025	0.723	2.81	0.606	0.914	2.83	1.258	0.343	0.901
50 [75]	3.37	0.692	0.712	3.45	0.338	0.931	3.48	0.781	0.362	0.944
60 [25]	2.52	0.058	0.898	2.88	0.028	0.963	3.54	0.020	0.452	0.993
60 [50]	2.78	0.142	0.801	2.99	0.076	0.932	3.32	0.076	0.388	0.982
60 [75]	3.79	0.644	0.601	3.90	0.248	0.859	4.10	0.579	0.290	0.941
60 [100]	3.14	1.320	0.891	3.20	0.620	0.958	3.18	1.033	0.470	0.918
70 [75]	3.88	0.285	0.646	4.07	0.115	0.892	4.37	0.214	0.324	0.976
PM41A30 for desorption										
60 [75]	4.25	0.025	0.976	5.87	0.003	0.963	3.83	0.030	1.535	0.999
60 [85]	3.89	0.052	0.974	4.64	0.013	0.946	3.78	0.054	1.437	0.990
60 [95]	3.88	0.106	0.980	4.25	0.037	0.944	3.85	0.106	1.250	0.986
60 [105]	3.96	0.157	0.984	4.21	0.062	0.922	3.94	0.155	1.324	0.995
PM41A40 for adsorption										
50 [75]	3.16	0.711	0.641	3.24	0.344	0.888	3.34	0.742	0.313	0.943
70 [75]	3.70	0.308	0.648	3.88	0.126	0.887	4.21	0.217	0.314	0.966

As shown in Table 3, based on the values of R^2>0.9, Avrami's fractional-order model presents a highly precise description of the adsorption behavior of all adsorbents. Furthermore, Avrami's kinetic constant k_A, i.e., self-equilibrium rate, can be used to demonstrate which adsorption is faster under the same reaction mechanism, which is appropriate for the condition described in this study and defined by the little-observed variation of n_A (0.275-0.362) [39].

It is well known that the more the PEI loaded, the slower is the self-equilibrium rate. As clearly seen in Fig. 13, the more the PEI loaded, the steeper is the slope of the second adsorption stage for M41-yP and PM41A30-yP, and the further it is from equilibrium. However, the difference is that, when the PEI loading rate is increased from 50 to 60 wt%, the variation amplitude of self-equilibrium rate differs between M41-yP and PM41A30-yP, with 65.8% and 25.9%, respectively. This is, of course, attributed to the fact that PEI coating emerged on M41 but not on PM41A30. However, as the PEI loading increased, the PEI coating appeared on PM41A30, which led to a sharp decrease in the self-equilibrium rate by 63%.

By applying Avrami's kinetic rate constant K_A obtained at different temperatures for PM41A30-60P, we obtained the linearized Arrhenius plot of $\ln(K_A)$ versus 1,000/T, as shown in Fig. 14. E_a calculated from the negative slope is positive, indicating that the adsorption rate increased with increasing temperature [38,59]. The positive temperature dependence of adsorption kinetics has been repeatedly reported, as clearly seen in Table 4. Negative activation energy is frequently observed, such as the adsorption of CO_2 on IG-MWCNTs [78], ZT-7 [4], and MFZ-700 [81]. The E_a value in this study was 51.76 kJ mol^{-1}, slightly smaller than the value of 62.24 kJ mol^{-1} obtained by Serna et al. [23], who used PEI-impregnated PM41. The reduced value obtained in this study is attributed to the difference in the CO_2 vol% of the feed between this and the reference (100% versus 5%) [78,81] studies.

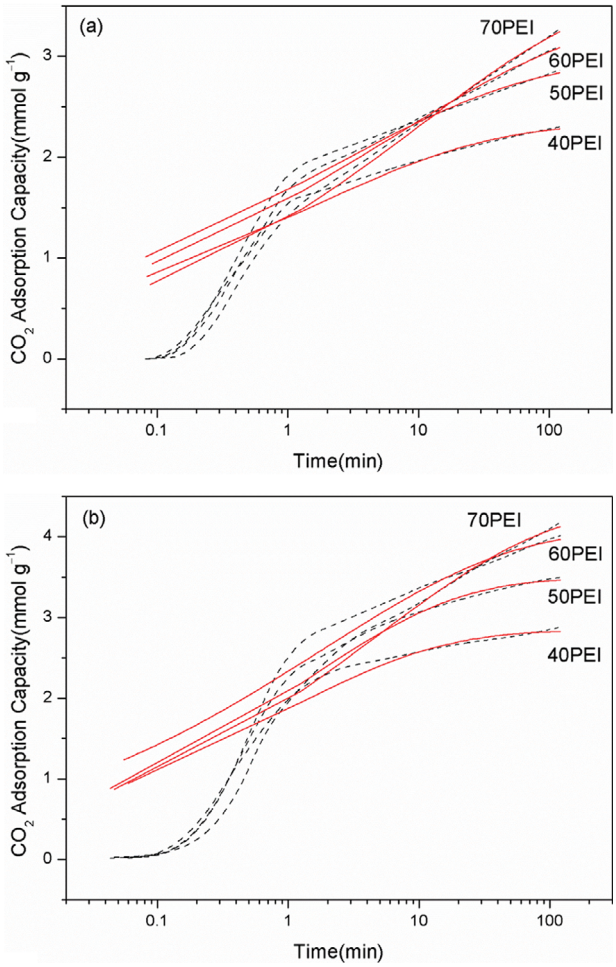

Fig. 13. Time-dependent profiles of CO_2 adsorption capacity at different PEI loadings for (a) M41-yP and (b) PM41A30-yP (solid lines: Avrami's fractional-order model, dashed lines: experimental data). Experimental conditions: pure CO_2 stream; flow rate=100 mL min^{-1}; adsorption temperature= 75 °C; and time duration=120 min.

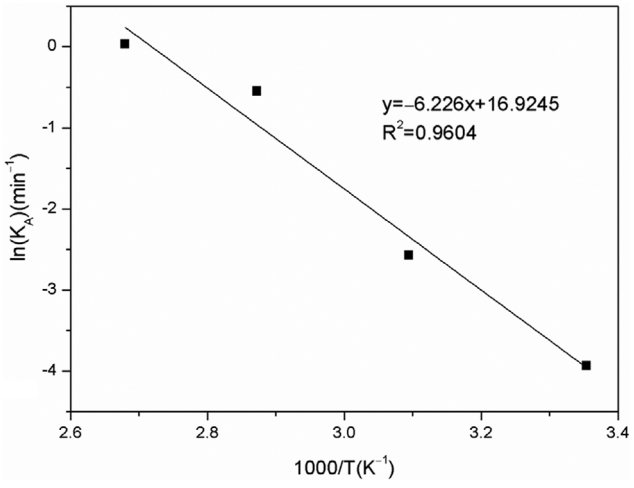

Fig. 14. Adsorption experiment data for PM41A30-60P at 25, 50, 75, and 100 °C; its linearized Arrhenius plot based on the Avrami's kinetic constant K_A.

Table 4. Activation energy (E_a) for PM41A30-60P and other adsorbents available in literature

Adsorbents (CO_2 vol%)	Temp range (°C)	E_a (kJ mol^{-1})	Reference
C-700 [a] (10%)	100-30	7.70	[60]
C-700 [a] (20%)	100-30	9.05	[60]
C-700 [a] (50%)	100-30	9.88	[60]
C-700 [a] (100%)	100-30	9.87	[60]
MEA	45-15	41 (62) [b]	[82]
IG-MWCNTs [a] (2%)	70-20	−13.2	[78]
IG-MWCNTs [a] (6%)	70-20	−12.98	[78]
IG-MWCNTs [a] (10%)	70-20	−7.35	[78]
IG-MWCNTs [a] (20%)	70-20	−6.72	[78]
IG-MWCNTs [a] (30%)	70-20	−5.88	[78]
IG-MWCNTs [a] (40%)	70-20	−3.68	[78]
IG-MWCNTs [a] (40%)	70-20	−3.02	[78]
ZT-7 [a] (10%)	100-40	−10.2	[4]
ZT-7 [a] (100%)	100-40	−13.6	[4]
CB-FM [a] (10%)	70-18	24 (34) [b]	[39]
Yellow tuff (10%)	70-25	14.4	[59]
MFZ-700 [a] (5%)	75-30	−4.8	[81]
MFZ-700 [a] (7%)	75-30	−3.1	[81]
MFZ-700 [a] (10%)	75-30	−3.3	[81]
MFZ-700 [a] (12.5%)	75-30	−3.8	[81]
SBA-15-33PEI (15%)	45-15	33.2	[75]
PM41-50TRI (5%)	70-25	1.38	[23]
PM41-50P (5%)	70-25	62.24	[23]
PM41-30P (100%)	75-25	-	[73]
PM41-50P (100%)	75-50	-	[73]
PM41A30-60P (100%)	75-25	51.76 (61.3) [b]	This study

3-2. Rate-limiting Mechanism Analysis

Because apparent kinetic models [39] were unable to predict the actual rate-limiting conditions, we employed three already established kinetic diffusion-controlled models to gain insight into the determining mass transfer resistance for adsorbing CO_2 on the adsorbents presented in this study. Generally, five consecutive steps are involved in the adsorption of CO_2 on porous solids [38,39,75]: (i) bulk diffusion—CO_2 molecules diffuse from the bulk gas phase to the gas film surrounding the adsorbent; (ii) film diffusion—CO_2 molecules cross the gas film surrounding the adsorbent to reach the external surface of the adsorbent; (iii) interparticle diffusion—CO_2 molecules diffuse inside the gaps among adsorbent monomers before entering the internal space of the adsorbent; (iv) intraparticle diffusion—CO_2 molecules shuttle through the amine layer inside the adsorbent pores; and (v) surface adsorption—CO_2 molecules react with the active sites adhering to the internal surface of the adsorbent. For an actual adsorption process, one or several of the above steps dominate the reaction rate, depending on the concrete conditions. Typically, bulk gas diffusion is instantaneously completed and frequently neglected [62].

Fig. 15(a) shows the interparticle diffusion model based on the experimental data of PM41A30-60P at 25, 50, 75, and 100 °C. The intercept of the linear part of the plot at each temperature is dis-

Table 5. Diffusion time constants obtained from pseudo-first-order kinetic constant (t_{D1}) and interparticle diffusion model (t_{D2})

Temp (°C)	Pseudo-first-order model		Interparticle diffusion model		
	k_1 (min^{-1})	t_{D1} (min^{-1})	Slope	Intercept	t_{D2} (min^{-1})
25	0.058	0.0039	−0.019	−0.610	0.0019
50	0.142	0.0095	−0.023	−0.894	0.0023
75	0.644	0.0429	−0.026	−1.590	0.0026
100	1.32	0.0880	−0.029	−2.245	0.0029

tinct from the value of $\ln(6/\pi^2)$, indicating that the interparticle diffusion process is not the step determining the reaction rate of CO_2 adsorption on PM41A30-60P [39]. Furthermore, as shown in Table 5, the diffusion time constants obtained from the pseudo-first-order kinetic constant (t_{D1}) and interparticle diffusion model (t_{D2}) differ. This confirms that interparticle diffusion is not the sole rate determinant [23].

Concerning intraparticle diffusion, the plot of q_t/q_e versus $t^{0.5}$ is not a straight line over the entire time frame at any investigated temperature. However, each curve can be approximated to three consecutive linear segments, corresponding to three different kinetic diffusion regions, namely A, B, and C, as shown in Fig. 15(b). Each is dominated by only one kinetic diffusion stage. As adsorption proceeds chronologically, it successively undergoes film diffusion, intraparticle diffusion, and equilibrium adsorption [62,75]. Therefore, multiple consecutively occurring kinetic diffusion processes collectively determine the adsorption of CO_2 on PEI-impregnated MCM-41-type adsorbents. In particular, film diffusion is the first kinetic diffusion stage encountered by CO_2. As seen in Fig. 15(b), the diffusion through the gaseous film surrounding the adsorbents lasts for only a short period for all temperatures, as also reported in previous studies [38,39]. For the following intraparticle diffusion, the duration is not only much longer but also highly temperature-dependent. The processes at 25 °C and 50 °C last longer than those at 75 °C and 100 °C. This phenomenon agrees well with the fact that, for heavily PEI-loaded adsorbents, the adsorption below 75 °C is dominantly controlled by diffusion, while a thermodynamically dominated one exists above 75 °C [73].

Moreover, no extended line of this segment passes the origin, illustrating that intraparticle diffusion is not the solely rate-limiting step. Finally, the adsorption enters a lasting equilibrium stage, distinguished from multiple known adsorbents such as activated carbon [39]. However, it is common for heavily PEI-loaded MCM-41-type adsorbents [27,67,75,80]. Generally, as adsorption deepens, an increasing number of active sites would be saturated. Consequently, the accessibility of the remaining sites becomes more difficult, especially for PEI, as illustrated earlier, thus resulting in a long-tail phenomenon at the equilibrium stage.

Fig. 15(c) shows the plot of B_t versus t based on the film diffusion model. The curves at all studied temperatures are not straight lines, again confirming that the intraparticle diffusion is not the rate-controlling step, and that film diffusion also participates in the control of adsorption from the overall perspective.

4. Generation Performance

As previously illustrated, because of the evaporation of PEI at temperatures of >130 °C, we chose 105 °C as the highest desorption temperature for a broader safety margin. Fig. 16 shows the time evolution of desorption performance in terms of desorption capacity, linearized desorption rate, and instantaneous desorption rate at 75, 85, 95, and 105 °C. As shown in Fig. 16(a), in the time frame of 120 min, the desorption ratio slightly increased as the temperature increased, which agrees with a previous report [73] that used PM41-50P as the adsorbent. Similarly, the desorption rate significantly increased as temperature increased, as shown in Figs. 16(b) and (c). Furthermore, as the temperature increased from 75 °C to 105 °C, the linearized desorption rate and maximum instantaneous desorption rate were magnified 5.5 and 6.2 times, respectively. Thus, the time required to accomplish the same desorption ratio distinctly varies at different temperatures. For instance, as the given temperature increased from 70 °C to 105 °C, the desorption time for 80% of total uptake was 9.2, 13.6, 25.8, and 47.1 min, respectively. This is because high temperatures increased CO_2 molecular mobility, activating them to desorb from the affinity sites and rapidly diffused away [39,83].

We employed the previously used apparent kinetic models to describe the desorption behavior. By comparing the value of R^2 listed in Table 3 and observing the deviation between experimental data and the fitted curve in Fig. 17, Avrami's fractional-order model still presents the best description of desorption data. The closest fitting in both adsorption and desorption by Avrami's model was reported by Raganati et al. [39] using a hybrid adsorbent. The kinetic rate constants K'_A increased 5.4 times as desorption temperature increased from 75 °C to 105 °C. The multiple growths are similar to the linearized desorption rate (5.5) and the maximum instantaneous desorption rate (6.2).

The kinetic constant K'_A was also applied to the Arrhenius equation, which generated a straight line with a negative slope, indicating the positive temperature dependence of desorption kinetics, as shown in Fig. 18. Consequently, the desorption activation energy was 61.3 kJ mol^{-1}, higher than that (51.76 kJ mol^{-1}) of adsorption, agreeing well with the exothermal nature of the CO_2-amine reaction [39,78,82].

To test the cyclic stability, we conducted five cycles of adsorption and desorption using PM41A30-60P. In particular, before the fresh adsorption, we exposed 10 mg of adsorbent to a 100 mL min^{-1} of flowing Ar at 105 °C for 60 min, then adjusted the temperature to 75 °C for the fresh adsorption under a 100 mL min^{-1} pure CO_2 flow for 120 min. After adsorption, we employed a two-step regeneration strategy. First, we increased the temperature to 105 °C and switched the feed to Ar, which was previously used to regenerate the loaded adsorbent for 60 min. As shown in Fig. 16(a), most of the desorption was completed during this period.

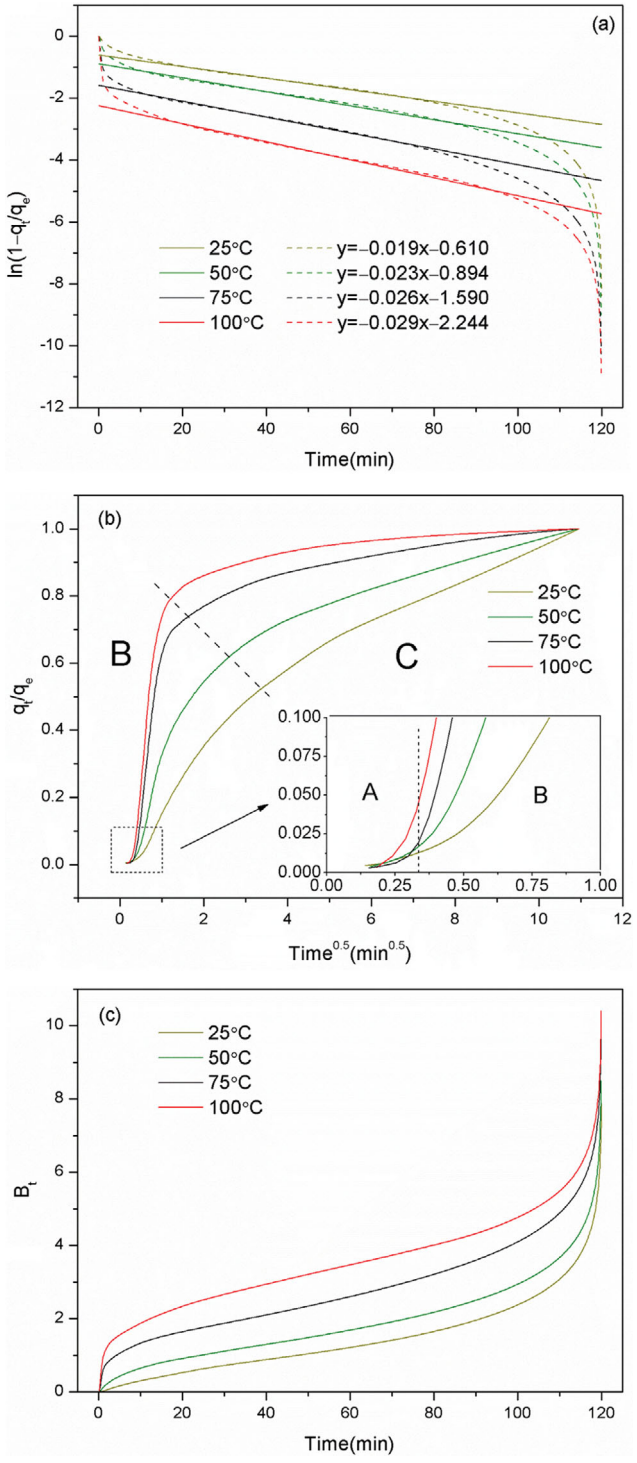

Fig. 15. Plots of (a) interparticle diffusion model, (b) intraparticle diffusion mode, and (c) film/boundary diffusion model based on the experimental data of PM41A30-60P at 25, 50, 75, and 100 °C. Experimental conditions: pure CO_2 stream; flow rate=100 mL min^{-1}; and time duration=120 min.

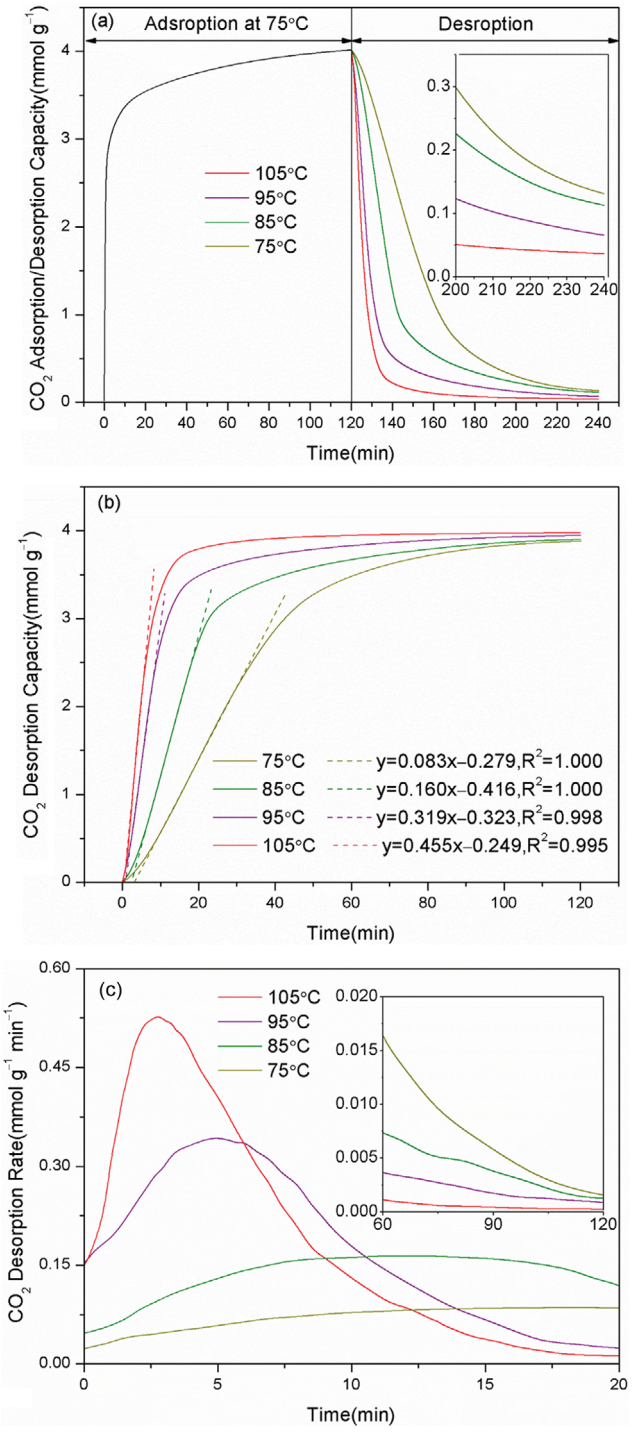

Fig. 16. Time evolution of loaded PM41A30-60P from the aspect of (a) desorption capacity, (b) linearized desorption rate, and (c) instantaneous desorption rate. Experimental conditions: pure argon stream; flow rate=100 mL min^{-1}; desorption temperature=75, 85, 95, and 105 °C; and time duration=120 min.

Second, we set the temperature target to 75 °C while maintaining the Ar purge. The convectional cooling proceeded along with low-temperature regeneration, lasting for 60 min. The fresh cycle ended and the regenerated adsorbent was ready for the next adsorption cycle. The following steps and experimental parameters are identical to the previous ones. As seen in Fig. 19 and Table 6, the working capacity, representing the actual amount of adsorbed CO_2 per cycle [38], retained a relatively high value after five cycles. The loss

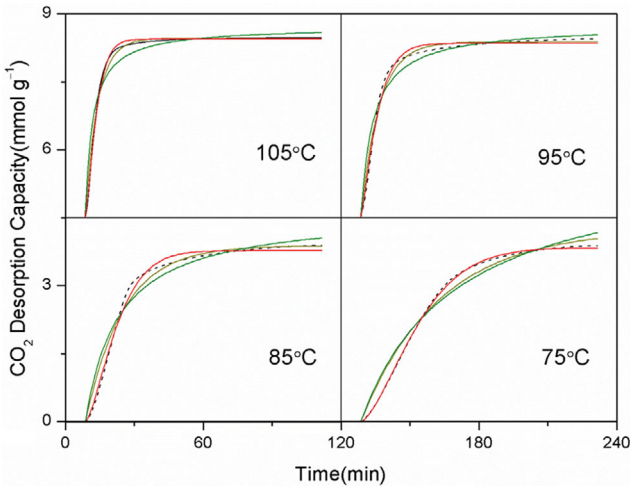

Fig. 17. Desorption data for PM41A30-60P at 75, 85, 95, and 105 °C and the fitting to kinetic models (dark yellow solid lines: Pseudo-first-order model; solid olive lines: pseudo-second-order model; solid red lines: Avrami's fractional-order model; dashed lines: experimental data). Experimental conditions: pure argon stream; flow rate=100 mL min^{-1}; and time duration=120 min.

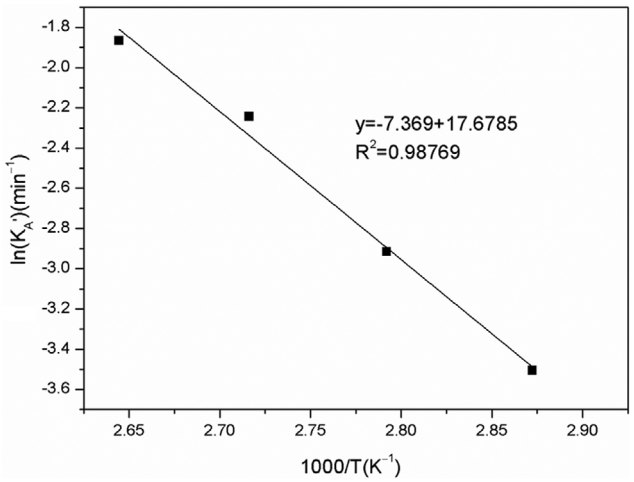

Fig. 18. Desorption data for loaded PM41A30-60P at 75, 85, 95, and 105 °C and its linearized Arrhenius plot based on Avrami's kinetic constant K_A'.

of working capacity was <5%. Here, we can conclude that (i) no deterioration of pore structure and loss of PEI occurred during the five cycles, and (ii) the regeneration was relatively thorough, thus promising the following working capacity. As a confirmation of the aforementioned conclusions, Table 6 lists the desorption ratio, almost >99% for desorption at 105 °C.

5. Comparison with other Adsorbents and Technical Feasibility for Practical Applications

To evaluate the application potential of the low-Si/Al-ratio adsorbents presented in this study, several representative adsorbents from the literature, including DEA, TRI, TEPA, PEI, silica gel, activated carbon, zeolites, and MOFs, were compared, as shown in Table 7. All cited adsorbents are the best-performing in the corresponding reference and exhibit the optimal adsorption performance at the given temperature. Traditional commercially popularized zeolite- and activated carbon-type adsorbents exhibit their best adsorption performance at ~25 °C. However, when they are exposed to relatively high temperature, the adsorption performance is considerably compromised. However, under a pressurized atmosphere, MOFs show extraordinary adsorption capacity for CO_2, several times that of zeolites. Among multiple MOFs, MIL-101 achieves the milestone capacity of 40 mmol g^{-1} at 50 bar and 30 °C. However, most MOFs are restricted by their considerably decreased uptake at a low partial pressure of 0.1-0.2 bar and poor selectivity when dynamically capturing CO_2. These unfavorable conditions for MOFs are frequently encountered in most industrial processes. Therefore, MOFs have not been commercially accepted. Nevertheless, many amine-containing species and well-characterized porous solids perform better at high temperature and low CO_2 partial pressure. This characteristic makes them an extraordinary choice for CO_2 post-combustion capture suitable for the predominant CO_2 emission source, namely coal-fired power plants [37,38]. Among multiple candidates acting as solid supports such as SBA-15, HMS, MCF, MCM-48, and MSU-J, MCM-41-type materials are competitive because of not only their well-defined adsorption-favorable pore structure, outstanding thermal, hydrothermal (after framework-substitution), and mechanical stability, and easily substituted framework and modified surface, but also the widely available sources, easily controlled preparation process, moderate synthesis conditions, and broadly regulatable synthesis parameters. Based on these advantages, we upgraded the reported MCM-41-type adsorbents by pore expansion treatment, incorporation of more heteroatom Al, and PEI loading optimization, which was then accomplished by higher adsorption capacity and faster kinetics. Compared to other adsorbents, PM41A30-60P always shows appreciable superiority in adsorption capacity, adsorption rate, or both.

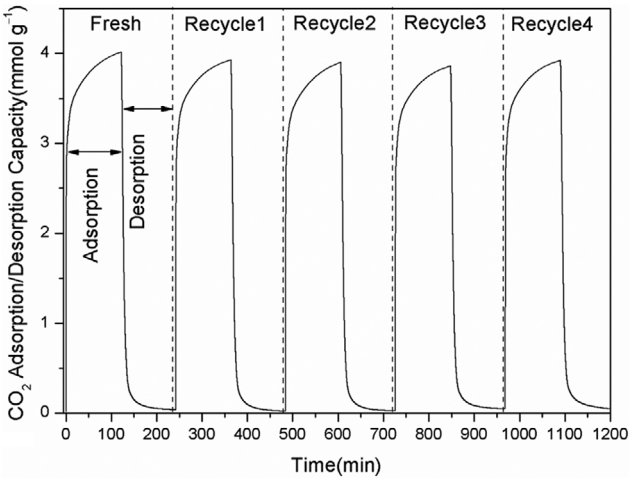

Fig. 19. Five consecutive cycles of adsorption and desorption for PM41A30-60P. Experimental conditions: for adsorption: pure CO_2 stream; flow rate=100 mL min^{-1}; temperature=75 °C; and time duration=120 min, and for desorption: pure argon stream; flow rate=100 mL min^{-1}; temperature=105 °C; and time duration=120 min.

The outstanding static adsorption performance exhibited by

Table 6. CO_2 cyclic adsorption-desorption data for PM41A30-60P

Temp (°C)	Cycle	Adsorption equilibrium (mmol g^{-1})	Desorption equilibrium (mmol g^{-1})	Desorption capacity[a] (mmol g^{-1})	Desorption ratio (%)[b]	Working capacity[c] (mmol g^{-1})	Adsorption ratio (%)[d]
105	Fresh	4.01	0.036	3.98	99.1	4.01	1
	2nd	3.92	0.021	3.90	99.5	3.89	96.9
	3rd	3.90	0.025	3.87	99.3	3.88	96.6
	4th	3.86	0.046	3.81	98.8	3.83	95.5
	5th	3.92	0.041	3.88	99.0	3.87	96.5
95	Fresh	4.01	0.066	3.95	98.4	-	-
85	Fresh	4.01	0.113	3.90	97.2	-	-
75	Fresh	4.01	0.131	3.88	96.7	-	-

[a]Desorption capacity is defined as the amount of CO_2 desorbed from the adsorbent and obtained by subtracting desorption equilibrium data from adsorption equilibrium data.
[b]Desorption ratio is the ratio of desorption capacity to the adsorption equilibrium data at the same cycle.
[c]Working capacity is characterized by the difference between the adsorption equilibrium data of the present cycle and the desorption equilibrium data of the prior cycle [38]. Thus, for the fresh cycle, the working capacity is the adsorption equilibrium data.
[d]Adsorption ratio is the ratio of the working capacity of each cycle to the fresh one. For the fresh cycle, the adsorption ratio is equal to 1.

PM41A30-60PEI provides a bright prospect for its practical application. However, when considering dynamic adsorption, some issues need to be addressed. A critical point is the particle size of the adsorbent, which determines the subsequent reactor configuration and detailed operating parameters. As shown in Fig. 5, the mean particle diameter of PM41A40-60P, the best-performed adsorbent in this study, is ca. 1.5 μm, which falls in the Geldart Group C (<30 μm) classification [89], i.e. fine powders with high adhesive forces between particles. Strong interparticle forces, mainly van der Waals, electrostatic, and moisture-related surface tension forces, pose a tremendous challenge to using a fluidized-bed reactor [90]. Although we can use a fixed-bed reactor for TSA, the pelletized adsorbents have a sharply reduced gas-solid interface and additional interior diffusion resistances. Based on the study of Raganati et al. [38], we can employ sound-assisted fluidized-bed technology. They used the same order of magnitude particle size of activated carbon (one-digit micron order) to achieve successful CO_2 dynamic adsorption. We advocate an additional modification to the sound-assisted fluidized-bed reactor by adding an immersed snake tube heat exchanger. It can contact with floating powder efficiently and ensure the isothermal condition that is difficult for PEI-loaded silica to achieve [91]. The combination of a heat exchanger with the existing apparatus is technologically feasible by side-introduction. Thus, the adsorbents presented in this study are technologically viable for practical application, and the specific implementation will be addressed in the next study.

CONCLUSIONS

PEI was impregnated in three MCM-41-type supports, M41, PM41, and PM41Ax, to investigate CO_2 adsorption at various PEI loadings and Si/Al molar ratios. At the same PEI loading rate, PM41-supported PEI outperforms its M41 counterpart in terms of adsorption capacity and adsorption rate. When PEI loading exceeds 50 wt%, the pore expansion increments are magnified to 15.9% and 21.3%, respectively. Because of the additional physisorption by exchangeable cations from alumina doping, using high-Al-content PM41Ax increases the adsorption capacity by 13.4% and the adsorption rate by 9.6%.

Concerning the effect of the Si/Al molar ratio, at 50 wt% PEI loading, the adsorption capacity is solely determined by the Al content of the support, exhibiting a negative dependence on the Si/Al ratio. While at 70 wt% PEI loading, the adsorption capacity is influenced by both PEI efficiency and Al content, reaching a maximum at the Si/Al ratio of 30.

A temperature-dependent study (25, 50, 75, and 100 °C) indicates that high temperatures always favor faster kinetics. Despite the exothermic process of CO_2-amine bonding, the adsorption capacity peaks at 75 °C. The adsorption activation energy of 51.76 kJ mol^{-1} agrees with data from previous studies. In addition, the presence of water vapor positively influences the adsorption capacity of PM41A30-60P.

Avrami's kinetic model accurately describes all experimental data, indicating hybrid adsorption. From an overall perspective, adsorption is controlled by a series of consecutively occurring kinetic diffusion steps. However, each diffusion stage is dominated by a single diffusion resistance. One important rate-controlling step is intraparticle diffusion. An inverse relationship exists between temperature and time dimension over the entire diffusion process. Furthermore, equilibrium adsorption exhibits a noticeable long-tail phenomenon in all investigated temperatures.

For PM41A30-60P, the generation temperature of 105 °C results in a desorption ratio of up to 99%. Thus, the adsorbent retains 95% of its initial adsorption capacity after five adsorption-desorption cycles. The desorption activation energy of 61.3 kJ mol^{-1} is larger than that of adsorption, which corresponds to the exothermicity of CO_2-amine bonding.

Finally, adsorption capacity and adsorption rate comparisons with this series of adsorbents and other classes show that the low-Si/Al ratio pore-expanded MCM-41-type adsorbents presented in this study are superior.

Table 7. Comparison of CO_2 adsorption performance between PM41A30-60P and other adsorbents

Adsorbent	Temp (°C)	Pressure (atm)	Uptake (mmol g^{-1})	Rate (mmol g^{-1} min^{-1})	Reference
Activated carbon	20	1	2.92		[84]
AAC[a]	20	1	3.22		[84]
NAC[a]	20	1	3.49		[84]
HAS[a]	20	1	3.75		[84]
MOF-505	25	1	3.3		[85]
MOF-177	25	35	33.5		[86]
MIL-101	30	50	40		[87]
13X Zeolite	25	1	3.82		[88]
4A Zeolite	25	1	3.07		[88]
Activated carbon	25	1	2.5		[88]
M41-40BZA[b]	25	1	0.91		[19]
M41-40MEA[b]	25	1	1.47		[19]
M41-40AEEA[b]	25	1	2.34		[19]
PM41-DEA[b]	25	0.05	2.57		[32]
PM41-DEA[b]	25	1	2.48		[32]
13X Zeolite	25	0.05	3.25		[32]
13X Zeolite	25	1	4.35		[32]
PM41-TRI[b]	25	0.05	1.41	0.96^{M}	[25]
M41-TRI[b]	25	0.05	0.91	0.84^{M}	[25]
13X Zeolite	25	0.05	2.05	0.88^{M}	[25]
ZSM-5-TEPA[b]	100	0.1	1.49		[4]
ZSM-5-TEPA[b]	100	1	1.8		[4]
ZSM-5-PEP	120	1	1.96		[5]
M41-50P	75	1	2.75	3.82^{L}	[34]
M41A100-50P	75	1	2.89		[34]
Silica gel-PEI	75	1	1.78		[34]
MCF-50PEI	75	1	3.91	1.92^{L}	[74]
HMS-50PEI	75	1	2.99	1.69^{L}	[74]
MSU-J-50PEI	75	1	3.15	1.65^{L}	[74]
SBA-15-50PEI	75	1	1.61	1.32^{L}	[74]
MCF-65PEI	75	1	4.57		[74]
HMS-65PEI	75	1	4.10		[74]
MSU-J-65PEI	75	1	3.64		[74]
SBA-15-65PEI	75	1	3.35		[74]
KIT-6-50PEI	75	1	3.07	2.98^{L}	[67]
Pure PEI	75	1	1.82	1.8^{L}	[67]
PM41A30-60P	75	1	4.01	4.26^{M} 4.13^{L}	This study

[a]AAC, NAC, and HAS are surface-modified activated carbons, respectively, by ammonia impregnation, microwave irradiation in the nitrogen and hydrogen atmosphere.
[b]BZA, MEA, DEA, AEEA, TRI, and TEPA are benzylamine, monoethanolamine, diethanolamine, N-(2-aminoethyl) ethanolamine, 3-[2-(2-aminoethylamino)ethylamino]propyltrimethoxysilane, and tetraethylenepentamine, severally.
[M,L]The adsorption rates with superscript M and L are the maximum instantaneous adsorption rate and linearized adsorption rate, individually.

ACKNOWLEDGEMENTS

The authors gratefully acknowledge the funded support by the National Key Research and Development Project (No. 2017YFB 0304001, No. 2017YFB0304201 and No. 2017YFB0304202) and Fundamental Research Funds for the Central Universities (N182508027).

REFERENCES

1. N. MacDowell, N. Florin, A. Buchard, J. Hallett, A. Galindo, G. Jackson, C. S. Adjiman, C. K. Williams, N. Shah and P. Fennell, *Energy Environ. Sci.*, **3**, 1645 (2010).
2. J. Wang, L. Huang, R. Yang, Z. Zhang, J. Wu, Y. Gao, Q. Wang, D.

O'Hare and Z. Zhong, *Energy Environ. Sci.*, **7**, 3478 (2014).
3. J. Przepiórski, M. Skrodzewicz and A. W. Morawski, *Appl. Surf. Sci.*, **225**, 235 (2004).
4. Y. Wang, T. Du, Y. Song, S. Che, X. Fang and L. Zhou, *Solid State Sci.*, **73**, 27 (2017).
5. Y. Wang, T. Du, Z. Qiu, Y. Song, S. Che and X. Fang, *Mater. Chem. Phys.*, **207**, 105 (2018).
6. Y. Wang, T. Du, H. Jia, Z. Qiu and Y. Song, *Solid State Sci.*, **86**, 24 (2018).
7. A. Sayari, Y. Belmabkhout and R. Serna-Guerrero, *Chem. Eng. J.*, **171**, 760 (2011).
8. Q. Yan, Y. Lin, C. Kong and L. Chen, *Chem Commun (Camb)*, **49**, 6873 (2013).
9. F. Liu, S. Chen, Y. Gao and Y. Xie, *J. Appl. Polym. Sci.*, **134**, 45046 (2017).
10. A. E. I. Elkhalifah, S. Maitra, M. A. Bustam and T. Murugesan, *Appl. Clay Sci.*, **83-84**, 391 (2013).
11. L. Ma, R. Bai, G. Hu, R. Chen, X. Hu, W. Dai, H. F. M. Dacosta and M. Fan, *Energy Fuels*, **27**, 5433 (2013).
12. X. Zhao, X. Hu, G. Hu, R. Bai, W. Dai, M. Fan and M. Luo, *J. Mater. Chem. A*, **1**, 6208 (2013).
13. Z. Zhou, C. M. Anderson, S. K. Butler, S. K. Thompson, K. J. Whitty, T. C. Shen and K. J. Stowers, *J. Mater. Chem. A*, **5**, 10486 (2017).
14. S. Das, A. Maity, M. Pradhan and S. Jana, *Anal. Chem.*, **88**, 2205 (2016).
15. O. Leal, C. Bolívar, C. Ovalles, J. J. García and Y. Espidel, *Inorg. Chim. Acta*, **240**, 183 (1995).
16. H. Y. Huang, R. T. Yang, D. Chinn and C. L. Munson, *Ind. Eng. Chem. Res.*, **42**, 2427 (2003).
17. G. S. Attard, J. C. Glyde and C. G. Göltner, *Nature*, **378**, 366 (1995).
18. X. Wang, L. Chen and Q. Guo, *Chem. Eng. J.*, **260**, 573 (2015).
19. S. Mukherjee, Akshay and A. N. Samanta, *Adv. Powder Technol.*, **30**, 3231 (2019).
20. T. C. dos Santos, S. Bourrelly, P. L. Llewellyn, J. W. Carneiro and C. M. Ronconi, *Phys. Chem. Chem. Phys.*, **17**, 11095 (2015).
21. S. Ahmed, A. Ramli and S. Yusup, *Int. J. Greenhouse Gas Control*, **51**, 230 (2016).
22. Y. Belmabkhout and A. Sayari, *Adsorption*, **15**, 318 (2009).
23. R. Serna-Guerrero and A. Sayari, *Chem. Eng. J.*, **161**, 182 (2010).
24. P. J. E. Harlick and A. Sayari, *Ind. Eng. Chem. Res.*, **46**, 446 (2007).
25. P. J. E. Harlick and A. Sayari, *Ind. Eng. Chem. Res.*, **45**, 3248 (2006).
26. R. Serna-Guerrero, Y. Belmabkhout and A. Sayari, *Chem. Eng. J.*, **158**, 513 (2010).
27. X. Xu, C. Song, J. M. Andresen, B. G. Miller and A. W. Scaroni, *Energy Fuels*, **16**, 1463 (2002).
28. N. Rao, M. Wang, Z. Shang, Y. Hou, G. Fan and J. Li, *Energy Fuels*, **32**, 670 (2018).
29. X. Wang, W. Zeng, M. Song, F. Wang, X. Hu, Q. Guo and Y. Liu, *Chem. Eng. J.*, **364**, 475 (2019).
30. C. Chen, H. Xu, Q. Jiang and Z. Lin, *Energy*, **214**, 119093 (2021).
31. M. G. Yıldız, T. Davran-Candan, M. E. Günay and R. Yıldırım, *J. CO_2 Utilization*, **31**, 27 (2019).
32. R. S. Franchi, P. J. E. Harlick and A. Sayari, *Ind. Eng. Chem. Res.*, **44**, 8007 (2005).
33. A. Heydari-Gorji, Y. Belmabkhout and A. Sayari, *Langmuir*, **27**, 12411 (2011).
34. X. Xu, C. Song, J. M. Andrésen, B. G. Miller and A. W. Scaroni, *Micropor. Mesopor. Mater.*, **62**, 29 (2003).
35. V. G. Gomes and K. W. K. Yee, *J. Sep. Purif. Technol.*, **28**, 161 (2002).
36. J. Mérel, M. Clausse and F. Meunier, *J. Environ. Prog. Sustain. Energy*, **25**, 327 (2010).
37. L. Riboldi and O. Bolland, *Int. J. Greenhouse Gas Control*, **39**, 1 (2015).
38. F. Raganati, R. Chirone and P. Ammendola, *Ind. Eng. Chem. Res.*, **59**, 3593 (2020).
39. F. Raganati, M. Alfe, V. Gargiulo, R. Chirone and P. Ammendola, *Chem. Eng. J.*, **372**, 526 (2019).
40. A. Glotov, A. Vutolkina, A. Pimerzin, V. Nedolivko, G. Zasypalov, V. Stytsenko, E. Karakhanov and V. Vinokurov, *Catalysts*, **10**, 537 (2020).
41. F. Kang, Q. Wang and S. Xiang, *Mater. Lett.*, **59**, 1426 (2005).
42. G. Wang, Y. Wang, Y. Liu, Z. Liu, Y. Guo, G. Liu, Z. Yang, M. Xu and L. Wang, *Appl. Clay Sci.*, **44**, 185 (2009).
43. C. Du and H. Yang, *J. Colloid Interface Sci.*, **369**, 216 (2012).
44. C. Zhou, T. Sun, Q. Gao, A. Alshameri, P. Zhu, H. Wang, X. Qiu, Y. Ma and C. Yan, *J. Taiwan Inst. Chem. Engineers*, **45**, 1073 (2014).
45. S. Miao, Z. Liu, H. Ma, B. Han, J. Du, Z. Sun and Z. Miao, *Micropor. Mesopor. Mater.*, **83**, 277 (2005).
46. H. Yang, Y. Deng, C. Du and S. Jin, *Appl. Clay Sci.*, **47**, 351 (2010).
47. J. Jin, J. Ouyang and H. M. Yang, *Appl. Clay Sci.*, **99**, 246 (2014).
48. R. Panek, M. Wdowin, W. Franus, D. Czarna, L. A. Stevens, H. Deng, J. Liu, C. Sun, H. Liu and C. E. Snape, *J. CO_2 Utilization*, **22**, 81 (2017).
49. C.-c. Li, X.-c. Qiao and J.-g. Yu, *Mater. Lett.*, **167**, 246 (2016).
50. G.-B. Hong, R.-T. Ruan and C.-T. Chang, *Chem. Eng. J.*, **215-216**, 472 (2013).
51. L. Y. Lin and H. Bai, *Environ. Sci. Technol.*, **47**, 4636 (2013).
52. T.-H. Liou, *Chem. Eng. J.*, **171**, 1458 (2011).
53. J. Liu, X. Wei, J. Xue and H. Su, *Mater. Chem. Phys.*, **241**, 122355 (2020).
54. Y. Ma, H. Chen, Y. Shi and S. Yuan, *Mater. Res. Bull.*, **77**, 258 (2016).
55. S. Chiarakorn, T. Areerob and N. Grisdanurak, *Sci. Technol. Adv. Mater.*, **8**, 110 (2007).
56. H. Ziaei-Azad, J. M. Kolle, N. Al-Yasser and A. Sayari, *Micropor. Mesopor. Mater.*, **262**, 166 (2018).
57. X. Wang, X. Ma, C. Song, D. R. Locke, S. Siefert, R. E. Winans, J. Möllmer, M. Lange, A. Möller and R. Gläser, *Micropor. Mesopor. Mater.*, **169**, 103 (2013).
58. D. Wang, X. Wang, X. Ma, E. Fillerup and C. Song, *J. Catal. Today*, **233**, 100 (2014).
59. P. Ammendola, F. Raganati, R. Chirone and F. Miccio, *Powder Technol.*, **373**, 446 (2020).
60. C. Goel, H. Kaur, H. Bhunia and P. K. Bajpai, *J. CO_2 Utilization*, **16**, 50 (2016).
61. S. Loganathan, M. Tikmani, S. Edubilli, A. Mishra and A. K. *Chem. Eng. J.*, **256**, 1 (2014).
62. N. Álvarez-Gutiérrez, M. V. Gil, F. Rubiera and C. Pevida, *Chem. Eng. J.*, **307**, 249 (2017).
63. B. H. Hameed, I. A. W. Tan and A. L. Ahmad, *Chem. Eng. J.*, **144**, 235 (2008).

64. S. K. Jana, R. Nishida, K. Shindo, T. Kugita and S. Namba, *Micropor. Mesopor. Mater.*, **68**, 133 (2004).
65. J. Villarroel Rocha, D. Barrera and K. Sapag, *Topics Catal.*, **54**, 121 (2011).
66. M. Kruk, M. Jaroniec and A. Sayari, *Micropor. Mesopor. Mater.*, **35-36**, 545 (2000).
67. W.-J. Son, J.-S. Choi and W.-S. Ahn, *Micropor. Mesopor. Mater.*, **113**, 31 (2008).
68. G. Qi, Y. Wang, L. Estevez, X. Duan, N. Anako, A.-H. A. Park, W. Li, C. W. Jones and E. P. Giannelis, *Energy Environ. Sci.*, **4**, 444 (2011).
69. C. Zhou, Q. Gao, W. Luo, Q. Zhou, H. Wang, C. Yan and P. Duan, *J. Taiwan Inst. Chem. Engineers*, **52**, 147 (2015).
70. X.-W. Wu, H.-W. Ma, L.-T. Zhang and F.-J. Wang, *Appl. Surf. Sci.*, **261**, 902 (2012).
71. Q. Wang, J. Luo, Z. Zhong and A. Borgna, *Energy Environ. Sci.*, **4**, 42 (2011).
72. H. Sepehrian, S. J. Ahmadi, S. Waqif-Husain, H. Faghihian and H. Alighanbari, *J. Hazard. Mater.*, **176**, 252 (2010).
73. A. Heydari-Gorji and A. Sayari, *Chem. Eng. J.*, **173**, 72 (2011).
74. D. Wang, X. Wang, X. Ma, E. Fillerup and C. Song, *Catal. Today*, **233**, 100 (2014).
75. K. Ge, Q. Yu, S. Chen, X. Shi and J. Wang, *Chem. Eng. J.*, **364**, 328 (2019).
76. X. Xu, C. Song, B. G. Miller and A. W. Scaroni, *Ind. Eng. Chem. Res.*, **44**, 8113 (2005).
77. Y. Belmabkhout, R. Serna and A. Sayari, Adsorption of CO2-Containing Gas Mixtures Over Amine-Bearing Pore-Expanded MCM-41 Silica: Application for Gas Purification (2009).
78. Q. Liu, J. Shi, S. Zheng, M. Tao, Y. He and Y. Shi, *Ind. Eng. Chem. Res.*, **53**, 11677 (2014).
79. Y. Liu and X. Yu, *Appl. Energy*, **211**, 1080 (2018).
80. A. Heydari-Gorji, Y. Yong and A. Sayari, *Energy Fuels*, **25**, 4206 (2011).
81. D. Tiwari, C. Goel, H. Bhunia and P. K. Bajpai, *Sep. Purif. Technol.*, **181**, 107 (2017).
82. W. Conway, X. Wang, D. Fernandes, R. Burns, G. Lawrance, G. Puxty and M. Maeder, *J. Phys. Chem. A*, **115**, 14340 (2011).
83. N. Tlili, G. Grévillot and C. Vallières, *Int. J. Greenhouse Gas Control*, **3**, 519 (2009).
84. Z. Zhang, M. Xu, H. Wang and Z. Li, *Chem. Eng. J.*, **160**, 571 (2010).
85. B. Chen, N. W. Ockwig, A. R. Millward, D. S. Contreras and O. M. Yaghi, *Angew. Chem. Int. Ed. Engl.*, **44**, 4745 (2005).
86. A. R. Millward and O. M. Yaghi, *J. Am. Chem. Soc.*, **127**, 17998 (2005).
87. P. L. Llewellyn, S. Bourrelly, C. Serre, A. Vimont, M. Daturi, L. Hamon, G. De Weireld, J. S. Chang, D. Y. Hong, Y. K. Hwang, S. H. Jhung and G. Ferey, *Langmuir*, **24**, 7245 (2008).
88. R. V. Siriwardane, M.-S. Shen, E. P. Fisher and J. A. Poston, *Energy Fuels*, **15**, 279 (2001).
89. F. Raganati, P. Ammendola and R. Chirone, *KONA Powder Particle J.*, **32**, 23 (2015).
90. P. Ammendola, F. Raganati and R. Chirone, *Fuel Process. Technol.*, **134**, 494 (2015).
91. G. Schöny, F. Dietrich, J. Fuchs, T. Pröll and H. Hofbauer, *Powder Technol.*, **316**, 519 (2017).